

# Design and Performance of the XENON10 Dark Matter Experiment

E. Aprile,<sup>1,\*</sup> J. Angle,<sup>2,3</sup> F. Arneodo,<sup>4</sup> L. Baudis,<sup>2,3</sup> A. Bernstein,<sup>5</sup> A. Bolozdynya,<sup>6</sup> P. Brusov,<sup>6</sup> L.C.C. Coelho,<sup>7</sup> C.E. Dahl,<sup>6,8</sup> L. DeViveiros,<sup>9</sup> A.D. Ferella,<sup>3,4</sup> L.M.P. Fernandes,<sup>7</sup> S. Fiorucci,<sup>9</sup> R.J. Gaitskell,<sup>9</sup> K.L. Giboni,<sup>1</sup> R. Gomez,<sup>10</sup> R. Hasty,<sup>11</sup> L. Kastens,<sup>11</sup> J. Kwong,<sup>6,8</sup> J.A.M. Lopes,<sup>7</sup> N. Madden,<sup>5</sup> A. Manalaysay,<sup>2,3</sup> A. Manzur,<sup>11</sup> D.N. McKinsey,<sup>11</sup> M.E. Monzani,<sup>1</sup> K. Ni,<sup>11,†</sup> U. Oberlack,<sup>10</sup> J. Orboeck,<sup>3</sup> D. Orlandi,<sup>4</sup> G. Plante,<sup>1</sup> R. Santorelli,<sup>1</sup> J.M.F. dos Santos,<sup>7</sup> P. Shagin,<sup>10</sup> T. Shutt,<sup>6</sup> P. Sorensen,<sup>9</sup> S. Schulte,<sup>3</sup> E. Tatananni,<sup>4</sup> C. Winant,<sup>5</sup> and M. Yamashita<sup>1</sup>

(XENON Collaboration)

<sup>1</sup>*Department of Physics, Columbia University, New York, NY 10027, USA*

<sup>2</sup>*Department of Physics, University of Florida, Gainesville, FL 32611, USA*

<sup>3</sup>*Physik-Institut, Universität Zürich, Zürich, 8057, Switzerland*

<sup>4</sup>*INFN - Laboratori Nazionali del Gran Sasso, Assergi, 67010, Italy*

<sup>5</sup>*Lawrence Livermore National Laboratory, Livermore, CA 94550, USA*

<sup>6</sup>*Department of Physics, Case Western Reserve University, Cleveland, OH 44106, USA*

<sup>7</sup>*Department of Physics, University of Coimbra, R. Larga, 3004-516, Coimbra, Portugal*

<sup>8</sup>*Department of Physics, Princeton University, Princeton, NJ 08540, USA*

<sup>9</sup>*Department of Physics, Brown University, Providence, RI 02912, USA*

<sup>10</sup>*Department of Physics and Astronomy, Rice University, Houston, TX, 77251, USA*

<sup>11</sup>*Department of Physics, Yale University, New Haven, CT 06511, USA*

(Dated: January 16, 2010)

XENON10 is the first two-phase xenon time projection chamber (TPC) developed within the XENON dark matter search program. The TPC, with an active liquid xenon (LXe) mass of about 14 kg, was installed at the Gran Sasso underground laboratory (LNGS) in Italy, and operated for more than one year, with excellent stability and performance. Results from a dark matter search with XENON10 have been published elsewhere. In this paper, we summarize the design and performance of the detector and its subsystems, based on calibration data using sources of gamma-rays and neutrons as well as background and Monte Carlo simulations data. The results on the detector's energy threshold, energy and position resolution, and overall efficiency show a performance that exceeds design specifications, in view of the very low energy threshold achieved (<10 keVr) and the excellent energy resolution achieved by combining the ionization and scintillation signals, detected simultaneously.

PACS numbers: 95.35.+d, 29.40.Mc, 95.55.Vj

## Contents

<b>I. Introduction</b>	2	<b>Analysis</b>	10
		A. S1 & S2 Pulse Identification	10
		B. Event Position Reconstruction	11
		C. Basic Quality Cuts	12
<b>II. The XENON10 Detector</b>	2	<b>VI. The XENON10 Calibration Data Results</b>	13
A. Principle of Operation	2	A. Gamma Calibration	13
B. Electrodes Assembly and Electric Fields	3	1. S1 light yield and energy scale	13
C. PMTs and Calibration System	5	2. S2 yield and liquid xenon purity	14
D. Cryogenic System	6	3. Position-dependence of S1 and S2 Signals	14
E. Xe Purification and Recirculation System	7	4. Combined energy scale	15
F. Slow Control System	8	B. Neutron Calibration	16
<b>III. The XENON10 Shield</b>	8	C. Nuclear/Electron Recoil Discrimination	17
<b>IV. The XENON10 Data Acquisition System</b>	9	<b>VII. The XENON10 Dark Matter Search Data</b>	19
<b>V. The XENON10 Data Processing and</b>		A. Background reduction with fiducial volume selection	19
		B. Definition of anomalous events and cuts	20
		<b>A. The XENON10 Backgrounds</b>	21
		1. Gamma and Neutron Backgrounds from Data and MC Simulations	22
		2. Intrinsic backgrounds in LXe	23
		<b>Acknowledgments</b>	24

\*XENON Spokesperson (E. Aprile). Phone: +1-212-854-3258.

E-mail address: age@astro.columbia.edu.

†Corresponding author (K. Ni). Now at Physics Department, Shanghai Jiao Tong University, China. Phone: +86-21-34202904.

E-mail address: nikx@sjtu.edu.cn.

## I. INTRODUCTION

The XENON10 detector, a two-phase time projection chamber (TPC) containing 25 kg of pure liquid xenon (LXe), was built and operated as the first practical prototype of the XENON dark matter search program [1]. The R&D phase which culminated with the XENON10 TPC, involved several smaller size detectors, dedicated to study many of the properties and performance characteristics of a two-phase TPC in the energy regime relevant to the direct detection of dark matter particles scattering off Xe nuclei. The most important results obtained with these prototypes are published [2–5].

In addition, several technical developments carried out during this phase played an important role in establishing the feasibility of the XENON approach for dark matter detection. Among these, two are particularly important: a) the development by Hamamatsu Photonics of compact metal channel photomultipliers (PMTs) for the detection of the LXe scintillation light, with continuous improvement in quantum efficiency and radio-purity [6–8]; b) the development of a pulse tube refrigerator (PTR) optimized for LXe temperature [9] to achieve the required long-term stability of a cryogenics detector filled with a large LXe volume.

The goal of the XENON10 experiment was to demonstrate the achievable energy threshold, background rejection power and operation stability of a two-phase TPC at the 10 kg fiducial mass scale, prior to the realization of a 100 kg scale detector, originally proposed as unit module for a ton scale XENON dark matter search.

The fast-paced R&D effort did not emphasize materials radio-purity and XENON10 was built with largely off-the-shelf components, not screened or selected to minimize backgrounds. The TPC and its associated cryogenics, purification and data acquisition (DAQ) systems were developed and tested at the Nevis Laboratories of Columbia University prior to installation at the Italian Gran Sasso Underground Laboratory (LNGS) [10]. The commissioning of the XENON10 detector at LNGS started in April 2006. Following the completion of the shield system, source calibration and background data were acquired for several months, in stable conditions. A blind analysis of 58.4 live days of data, acquired between October 6, 2006 and February 14, 2007, and using a fiducial mass of 5.4 kg, excluded previously unexplored parameter space, setting improved upper limits on both spin-independent [11] and spin-dependent [12] cross-section for dark matter scattering off nucleons.

The XENON10 results, and the unusually fast time scale in which they were achieved, validated the scientific reach of a position sensitive, homogeneous and self-triggered LXeTPC for dark matter direct detection. New and improved LXe dark matter detectors, with a target mass at the 100 kg scale, are currently in operation [15]

or under construction [16, 17]. They promise to advance the field with significant improvement in sensitivity over the next few years. In this paper we wish to summarize the development and performance of the XENON10 detector and associated systems. The plan of the paper is the following. In Section 2 we describe the design of the detector, cryogenics, purification and slow-control systems, followed by a description of the shield and data acquisition systems. In Section 3 we discuss the data processing, the algorithms and cuts used to infer the parameters relevant for a dark matter search. In Section 4, we present results from gamma and neutron calibration of the XENON10 TPC. Finally in Section 5, details on the analysis of XENON10 data used for the published dark matter search results are discussed. The appendix to the paper deals with a summary of the sources of backgrounds in the XENON10 experiment, in comparison with Monte Carlo predictions.

## II. THE XENON10 DETECTOR

### A. Principle of Operation

The principle of operation of the XENON10 two-phase (liquid-gas) time projection chamber (TPC) is shown schematically in Fig. 1. The energy deposited by a particle interaction within the active LXe volume is detected by the simultaneous measurement of ionization electrons and of primary scintillation photons ( $S1$ ), with a wavelength of 178 nm [13], produced by the de-excitation to the ground state of excited diatomic Xe molecules ( $Xe_2^*$ ) [14]. Both direct excitation of atoms and electron recombination lead to the formation of  $Xe_2^*$ .

Under the application of an electric field,  $\varepsilon_d$ , on the order of 1 kV/cm, the electrons which escape recombination with the parent positive ions, drift towards the liquid-gas interface with a velocity of about 2 mm/ $\mu$ s. Once they reach the liquid surface, they are extracted into the gas, where a much stronger electric field,  $\varepsilon_e$ , accelerate them leading to secondary scintillation photons emission ( $S2$ ). In the XENON10 TPC, photomultiplier tubes (PMTs), coupled directly to the sensitive liquid and gas regions, are used to detect both  $S1$  and  $S2$  signals. As shown in [2], the extraction yield is 100% for a field greater than 10 kV/cm. The number of secondary scintillation photons emitted in the gas is proportional to the number of electrons, and thus to the energy deposited in the liquid by the incoming particle. We refer to this signal as proportional scintillation signal. The following equation expresses the dependence of this signal on the operation conditions:

$$N_\gamma = \alpha N_e (\varepsilon_e/p - \beta) p x. \quad (1)$$

Here  $p$  is the gas pressure and  $x$  is the distance traveled by the electrons in the gas which largely determines the width of the  $S2$  pulse. The units for  $p$ ,  $\varepsilon_e$  and  $x$  are bar, kV/cm and cm, respectively.  $N_e$  is the number of

electrons extracted from the liquid to the gas phase,  $N_\gamma$  is the number of proportional scintillation photons produced.  $\alpha$  (the amplification factor) and  $\beta$  (the threshold of the reduced field for proportional light production) are experimentally determined values. For the case of Xe, the reported values for  $\alpha$  vary from 70 to 140 and  $\beta$  values are between 0.8 and 1.0 kV/cm/bar [2, 18, 19]. The number of secondary photons generated by one drifting electron is sufficiently large to be detected by PMTs, thus a two-phase detector is single-electron sensitive. In XENON10 operating conditions, the values of  $p$ ,  $\epsilon_e$  and  $x$  were 2.1 bar, 12 kV/cm and 0.25 cm, respectively, yielding  $\sim 100$  photons per extracted electron.

The different amplitude of the  $S1$  and  $S2$  signals associated with nuclear recoils, such as produced by WIMP or neutron interactions, and with electron recoils, such as produced by background beta and gamma-rays, provides the basis for background discrimination in a two phase TPC such as XENON10. Since electron diffusion in LXe is small [20], the proportional scintillation pulse is produced in a small volume with the same  $XY$  coordinates as the interaction site, allowing 2D localization. The  $Z$  coordinate is inferred from the drift time measurement, and the known electron drift velocity at the operating field. The TPC approach and the strong self-shielding property of LXe ( $\rho \approx 3$  g/cc,  $Z = 54$ ), make the XENON concept very powerful for background identification and rejection based on event topology: multiple scatter events from the overwhelming majority of gamma rays and from neutrons can be identified and rejected. The sensitive target can be “fiducialized” to keep only the inner core free of background.

The capability to accurately identify the 3D position on an event-by-event basis, also allows to correct the position dependence of both the direct and proportional scintillation signals, which in turn results in improved energy resolution. For a recent review of the properties of LXe and its response to radiation we refer to [20].

One of the challenges of a two-phase detector is to efficiently detect the small number of primary scintillation photons associated with the low energy events of interest in a dark matter search. Because of the large refractive index of LXe [21] and consequent total internal reflection at the liquid/gas interface, the presence of PMTs at the bottom of the active drift volume is essential for efficient  $S1$  light collection.

When the XENON concept was proposed, the development of PMTs capable to operate directly in LXe had just began. The typical quantum efficiency of these early PMTs at 178 nm was in the 10% range. To achieve high light collection of the  $S1$  signal and thus a low energy threshold required for a dark matter search, the baseline XENON detector design used a CsI photocathode in place of a common cathode, and photomultipliers or other type of photodetectors in the gas region [22]. During the XENON R&D phase, different photodetectors were tested [23, 24] and also charge-sensitive readouts based on the Gas Electron Multiplier concept [25]. The

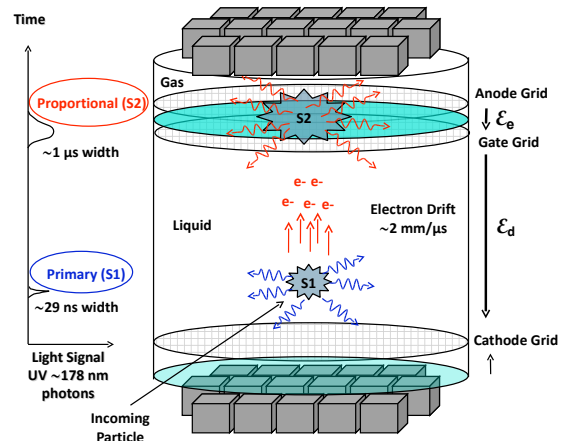


FIG. 1: (Color online) Principle of operation of the XENON10 two-phase TPC. A particle interaction in the liquid produces primary scintillation light ( $S1$ ) and ionization electrons. The electrons drift under an electric field  $\epsilon_d$  (about 1 kV/cm) until they are extracted from the liquid into the gas where they are accelerated by an electric field  $\epsilon_e$  (about 10 kV/cm) producing proportional scintillation light ( $S2$ ). Two arrays of photomultipliers, one in the liquid and one in the gas, detect simultaneously the  $S1$  and  $S2$  light signals.

operation of CsI photocathodes to detect the direct light in two phase prototypes confirmed [26] the high QE first measured by the Columbia group [27]. However, the complexity of operating a TPC under the very strong electric field required by the CsI photocathode, while suppressing positive photon feedback, and the fast improvement of the performance of Hamamatsu PMTs for LXe operation, led us to abandon the CsI photocathode approach. Prior to adopting the Hamamatsu one-inch square R8520 PMT for XENON10, a two-inch diameter R9288 PMT was extensively tested [2, 26].

## B. Electrodes Assembly and Electric Fields

Fig. 2 shows a 2D mechanical drawing of the XENON10 detector assembly, and Fig. 4 shows a picture of the detector mounted on the movable door of the passive shield (see section III). A closer view of the inner TPC structure is shown in Fig. 3. The TPC active volume is defined by a polytetrafluoroethylene (PTFE) cylinder with an inner diameter of 20 cm and a height of 15 cm for a total active mass of about 14 kg of LXe. PTFE is used as UV light reflector [28] and as electrically insulating support for the TPC structure.

To produce the electric fields in the liquid and gas regions, four wire meshes, also referred to as grids, are used; two in the liquid (cathode and gate grid) and two in the gas (anode and top grid). The 0.203 mm thick electroformed meshes, are made of electropolished 304 stain-

less steel, with a bar width of 0.182 mm and  $2.0 \text{ mm} \times 2.0 \text{ mm}$  square holes, insuring good optical transmission. The cathode, at the bottom of the PTFE cylinder, and the gate grid define the TPC 15 cm drift distance. Field shaping rings, made of 0.5 mm thick copper and spaced by 0.76 cm, are mounted outside the PTFE cylinder to insure a uniform electric field across the drift volume.

A 5 mm gap separates the gate grid from the anode and the anode from the top grid. The liquid level is between anode and gate grid and determines the extraction field. The liquid level, 2.5 mm above the gate grid, is kept constant by the use of a pressurized cylinder closed on the top, similar to a diving bell. The pressure is provided by the return of the gas circulating through the purifier (see Section II E). Custom-made capacitors are used to monitor the liquid level: one cylindrical capacitor is used to measure the liquid level and four parallel-plate capacitors are used to measure the inclination of the detector, to ensure that the liquid level is parallel to the grids and thus that the extraction field is uniform. One of the parallel-plate capacitors is filled with PTFE and is used as a reference capacitor: the capacitances of other parallel-plate capacitors are compared with the reference value to control the inclination of the detector. The XENON10 cryostat was equipped with leveling feet which could be adjusted from outside the shield structure to achieve the required degree of leveling.

To minimize passive LXe outside the TPC, the PTFE cylinder is surrounded by an outer PTFE cylinder, with cut-outs for the resistors of the voltage divider network, directly mounted on the field shaping wires. A photo of the assembled TPC structure, with the top three meshes clearly visible, is shown in Figure 5. For most of the data acquired with XENON10, the top and gate grids were biased to  $-1.15 \text{ kV}$ , with the anode and cathode at  $+3.5 \text{ kV}$  and  $-13 \text{ kV}$ , respectively. With these voltages, the drift field in the liquid was  $0.73 \text{ kV/cm}$  while the field in the gas was  $12 \text{ kV/cm}$ . The high voltage for the gate, anode, and top meshes was provided by CAEN 1733 and 1833 power supplies [29], while the higher voltage for the cathode was provided by a Heinzinger power supply [30]. Commercial HV feedthroughs and cables carried these voltages to the cryostat. To carry the high voltages from the vacuum of the cryostat to the cathode mesh, a custom-made PTFE insulated feedthrough was used. Inside the TPC structure and below the LXe level, bare wires were used to carry the HV to the upper meshes, taking advantage of the excellent dielectric properties of LXe and of PTFE.

Results from electric fields simulations for the XENON10 TPC are shown in Fig. 6, for a drift field of  $1 \text{ kV/cm}$ . The field is uniform up to 3 mm from the PTFE wall. For the dark matter search results, only events with at least 10 mm distance from the edge of the active volume were accepted. Gamma-ray calibration data confirmed that no charge was lost for events in this region. On the bottom of the detector, a region of reversed field direction exists between the cathode and the

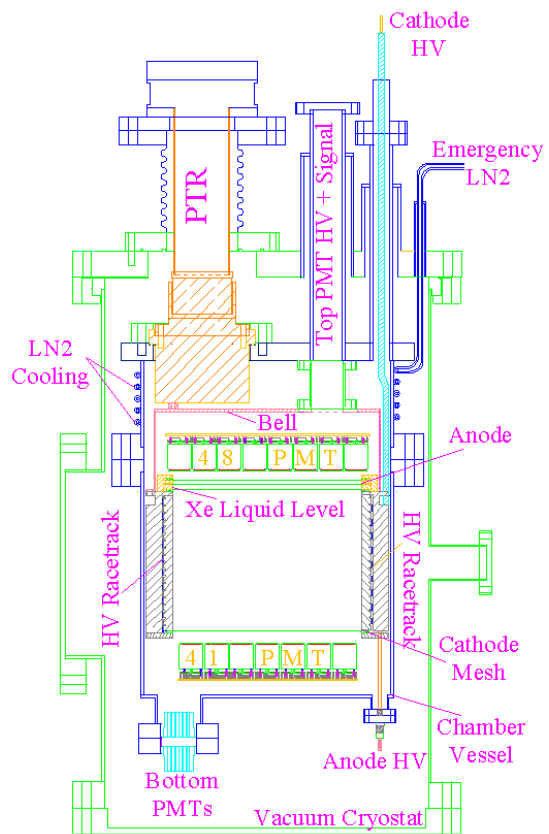


FIG. 2: (Color online) Schematic drawing of the XENON10 detector.

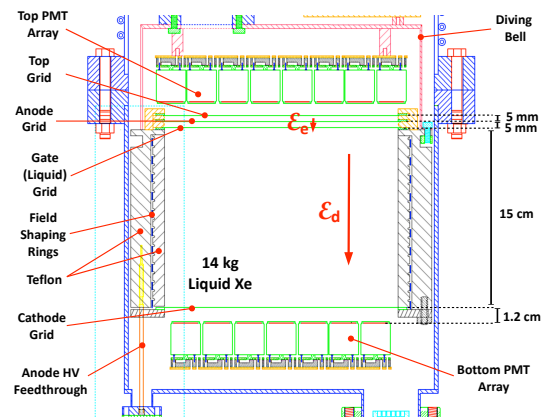


FIG. 3: (Color online) A close-up view of the XENON10 TPC structure.

bottom PMT array, separated by a distance of 1.2 cm. The field reversal extends slightly into the sensitive volume, affecting a region less than 0.9 mm above the cathode.

The same set of field simulations was used to establish that the displacement of the true  $XY$  event position



FIG. 4: (Color online) Photo of the XENON10 detector and shield, with the shield door open.

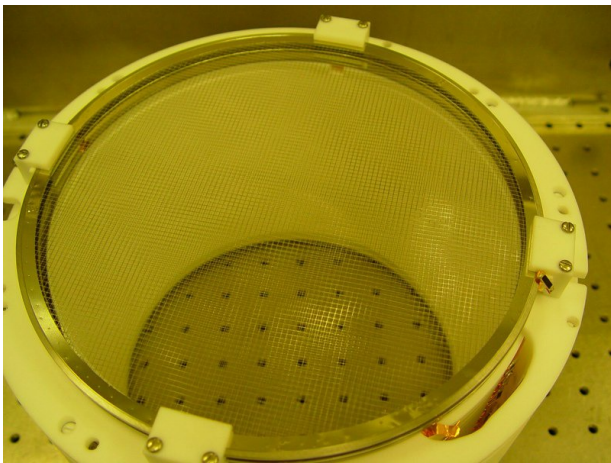


FIG. 5: (Color online) Photo of the assembled XENON10 TPC structure.

and the mean  $XY$  position from the proportional scintillation was negligible ( $< 0.6$  mm). The impact of the field distribution in the gas on the energy resolution of the detector was also studied. For the inner region of the meshes, it was found that the relative path length variation of electrons traversing the gap from the liquid-gas surface to the anode mesh is  $\leq 20\%$  FWHM.

### C. PMTs and Calibration System

The active LXe volume is viewed by 89 PMTs: the bottom array of 41 PMTs is located 1.2 cm below the cathode, fully immersed in LXe. The 48 PMTs of the top array are in the gas. The XENON10 PMTs are  $1'' \times 1''$  square Hamamatsu R8520-06-AL [31] designed to work in LXe and optimized for low radioactivity. They have a bialkali photocathode and a quartz window, with a typical quantum efficiency  $> 20\%$  at 178 nm. They are

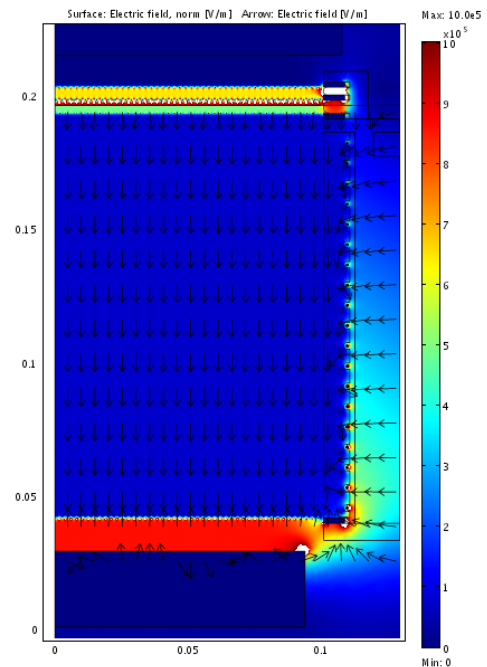


FIG. 6: (Color online) Simulated electrostatic field in XENON10. Arrows and colors indicate the field direction and strength, respectively. The field cage was optimized for field uniformity in the sensitive region. The region below the cathode shows a strong reversed field.

compact (only 3.5 cm tall), metal channel PMTs, with 10 multiplication stages and a total amplification of a few  $10^6$ . They are certified for operation at  $-100^\circ\text{C}$  and up to 5 bar. The radioactivity of these PMTs was measured with an ultra sensitive HPGe detector [32] at the Gran Sasso Low Background facility [33]. Their contamination in  $^{238}\text{U}/^{232}\text{Th}/^{40}\text{K}/^{60}\text{Co}$  was measured as low as  $(0.25 \pm 0.04)/(0.21 \pm 0.05)/(9.3 \pm 1.1)/(0.59 \pm 0.05)$  mBq/PMT.

A photo of the top array, mounted inside the “diving bell” structure which defines the liquid level, is shown in Fig. 7. The custom-made cathode HV feedthrough and the level meter are also visible. The high voltage for the PMTs is provided by CAEN 1833 power supply boards [29]; this system featuring single channel control, allowed to easily equalize the gain of the PMTs, by adjusting individual voltages.

The HV divider for the PMTs was mounted on a Cirlex substrate, with surface mount components. The Cirlex boards for each of the two arrays are mounted on copper plates with PTFE spacers for insulation. Despite the small mass, the ceramic of the resistors and capacitors contribute the largest fraction of the radioactive background of the HV divider boards. Heating of the LXe by the resistive dividers is kept to a minimum by choosing high resistance values (10 M $\Omega$ ), allowed because of the low event rate and low light level during dark matter search data-taking. The typical power consumption of the XENON10 PMTs was about 5 mW per PMT.

Negative HV was applied to the cathode of each PMT, via unshielded Kapton wire. The average HV was about 750 V, with a maximum of 900 V. The signal was carried out with 50  $\Omega$  teflon cables (RG178U), stripped of their shielding, to avoid trapped air which would impact the liquid purity. PMTs signal and HV cables were carried outside by 48 pin Burndy feedthroughs [34]. The radioactivity of these feedthroughs was reduced by replacing the ceramic plugs holding the pins with plugs made out of polyether ether ketone (PEEK).

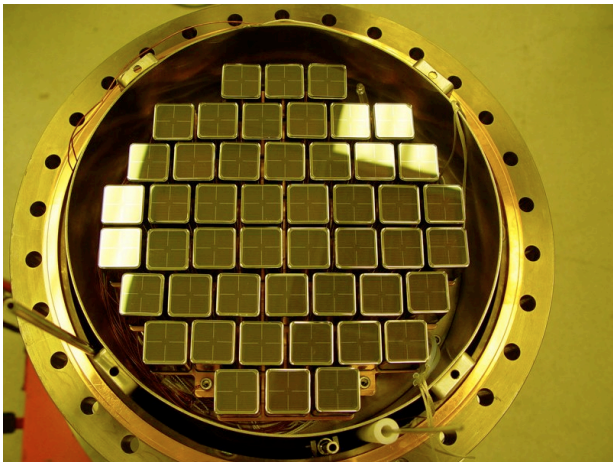


FIG. 7: (Color online) XENON10 top PMT array, with the cathode HV feedthrough and liquid level meter also visible.

The 89 PMTs were routinely calibrated with the goal of equalizing the gain and to correct for differences in the quantum efficiency. The gain equalization was performed using light emitting diodes (LEDs). Two LEDs were used: one was mounted close to the top array, to equalize the bottom PMTs; the other was mounted close to the bottom array, to equalize the top PMTs. Both LEDs were covered with a PTFE cap acting as a diffuser to ensure a uniform illumination of all the PMTs in each array. The LEDs were driven by a pulse generator, which synchronously activated also the main DAQ trigger: the pulse duration was 6  $\mu$ s, but the charge on each channel was integrated only in a 1  $\mu$ s window, 4  $\mu$ s after the activation of the LED, to minimize electronics noise generated when the LED was switched on.

The gain measurement was performed in single photoelectron (p.e.) regime. Under the assumption that the p.e. spectrum is the sum of a Gaussian noise peak and a Gaussian single p.e. peak, each with a Poisson-like distribution, and with a single photoelectron to noise ratio of 1/5, less than 2% of the events had 2 or more photoelectrons (a typical single p.e. spectrum is shown in figure 8). To ensure that the single p.e. condition was met for all the PMTs, the calibration data were acquired under different illumination conditions. The spectra for each PMT were fitted with a function which included the noise Gaussian, the single p.e. Gaussian and a third Gaussian accounting for the multiple p.e. contribution.

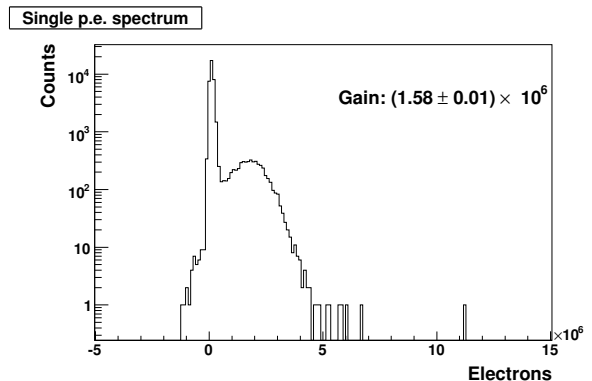


FIG. 8: Single photoelectron spectrum of a XENON10 top PMT, acquired during a routine LED calibration. Clearly visible is also the noise peak.

After measuring the gain for each channel, the amplification factor was equalized for all PMTs, by adjusting the single PMT operating voltage. After the equalization, the gains were measured again and the resulting amplification factors were then fed to the XENON10 data analysis programs (see Sec. V) and used as a conversion factor between the measured charge and the actual p.e. number. During normal operation, such a gain measurement was repeated at least once a week, to ensure the stability of the PMTs gain. The time evolution of the gain, measured during the WIMP search data taking, is shown in Fig. 9 for two typical PMTs. The variation in PMT gain was  $< 2\%$ .

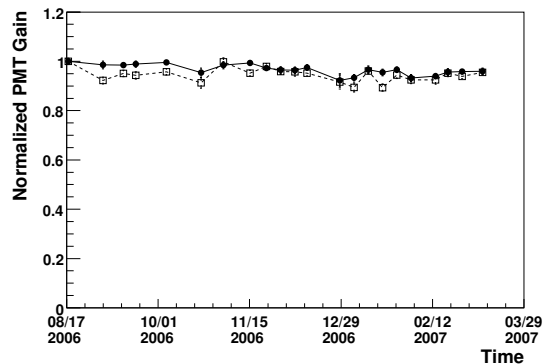


FIG. 9: Stability of the gain of two typical XENON10 PMTs during the WIMP search data taking period.

#### D. Cryogenic System

A reliable and stable cryogenics system was an essential requirement for the XENON10 experiment since both PMTs gain and the proportional light yield vary with temperature. The XENON10 TPC vessel containing the 25 kg of LXe, made of stainless steel (SS), was

wrapped with aluminized mylar and surrounded by a vacuum cryostat, also made of SS, with typical vacuum in the mTorr range. The cryogenics system was based on a Pulse Tube Refrigerator (PTR) with 100 W of cooling power at 165 K, with a 3.5 KW compressor. This type of cryocooler was developed specifically for Xe liquefaction and re-condensation in the LXe scintillating calorimeter of the MEG experiment [9]. To meet the ultra-high purity requirement for the XENON10 TPC, the cryocooler was placed outside of the detector vessel, mounted on the vacuum cryostat top flange and attached to a copper plate which worked as re-condenser for the evaporated Xe gas. The cooling power was sufficient to cool-down the detector, liquefy the gas and re-condense it. The desired temperature of the LXe was adjusted by a Proportional-Integral-Derivative (PID) controlled heating element on the cold head of the PTR. Due to the narrow temperature margin of less than 4 degrees between the liquid and solid phase of Xe, temperature control during liquefaction is especially important. The typical operating temperature for XENON10 was  $-94^{\circ}\text{C}$  with a stability better than  $0.05^{\circ}\text{C}$ . At this temperature the Xe vapor pressure is  $\sim 2.1$  atm. With this cryogenic system we have been able to achieve the level of long term stability required for a dark matter experiment. Fig. 10 shows the stability of the LXe temperature and corresponding Xe vapor pressure during several months of continuous operation of XENON10.

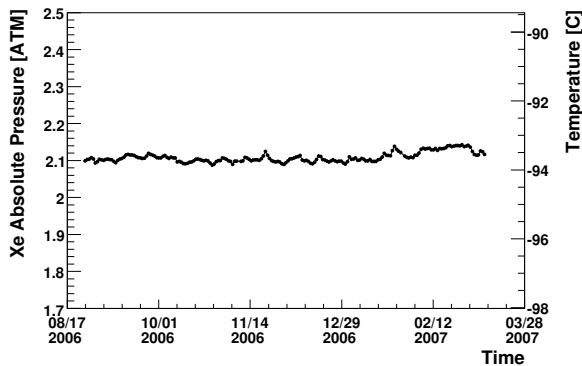


FIG. 10: Stability of the liquid Xe temperature and corresponding vapor pressure in the XENON10 detector during the calibration and WIMP search data-taking period.

The XENON10 cryogenics system included an independent  $\text{LN}_2$  system for emergency cooling. A pressure rise in the detector, above a set value, would automatically trigger a flow of  $\text{LN}_2$  through a cooling coil next to the PTR. The TPC pressure sensor and the solenoid valve control were powered by a dedicated uninterruptible power supply. The emergency cooling system would keep detector in a safe state even in the extreme case of power failure and no access to the laboratory for more than 24 hours. We note that the large Xe mass and high thermal capacity stabilizes the temperature and the pres-

sure against abrupt changes. A rupture disk would finally burst if the absolute pressure in the detector would rise above 3.5 atm, to avoid damage to the PMTs.

### E. Xe Purification and Recirculation System

The 15 cm electron drift gap in the XENON10 detector imposes ultra-high purity requirements on the LXe, in order to minimize charge loss by electron attachment to impurities molecules. The overall concentration of electronegative impurities (Oxygen equivalent) must be well below 1 part per billion (ppb). Moreover, stable operation of the detector demands that this high purity be maintained over long periods of time. For detector and gas system ultra high vacuum materials and procedures were used, and for cleaning the Xe gas a single purifier, a high temperature SAES getter (PS4-MT3-R) [35] was used.

However, the PMTs limited the bake-out temperature of the detector to  $70^{\circ}\text{C}$ . In addition, LXe is a good solvent due to Van der Waals interactions with impurity molecules. Thus, once pure Xe is liquefied in the detector, the purity level can easily deteriorate. We therefore implemented a closed circulation system to continuously clean the gas through the getter, after initial liquefaction. Such a system was successfully developed and tested at Columbia on several smaller scale prototypes, prior to adapting it to XENON10. For gas circulation a double-diaphragm pump (KNF-N143.12E) [36] was used. With a gas flow rate of 2.6 slpm, limited largely by the PTR cooling power, it would take about one month to reach the purity level required for negligible electron attenuation. A schematic of the gas purification and recirculation system used on XENON10 at LNGS is shown in Fig. 11.

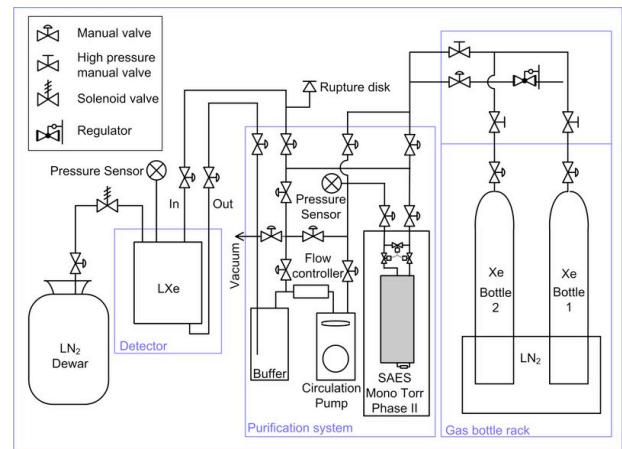


FIG. 11: Schematic of the Xe purification system with closed-loop re-circulation.

## F. Slow Control System

A Slow Control System (SCS) was developed to monitor all essential run-time parameters of the XENON10 experiment, controlling the status of various hardware components, triggering alarms and transmitting important parameters.

The SCS monitors over 290 parameters, which include gas pressure, cryogenic temperatures, flow rate, liquid level, grids and PMTs high voltages, DAQ trigger and acquisition rate, room temperatures and detector inclination. Figure 10 is an example of the detector parameters monitored by the SCS during the dark matter run.

The SCS consists of 4 parts: (i) server, (ii) monitor client, (iii) alarm client, and (iv) history plotter. The server establishes communication with all the different instruments monitored, makes all the parameters available for the clients, and stores the information to disk. The monitor client allows each user access to all the parameters monitored over the last 24 hours. The alarm client triggers the alarm system in case one of the preassigned parameters falls outside the allowed range. Alarms are sent via email and as text messages to the cell phones of the appropriate personnel. In addition to this automated system, the LNGS personnel continuously monitors the gas pressure. The history plotter allows the user to access the information stored for each parameter for any particular time.

The SCS is a platform independent software developed exclusively for the XENON10 experiment using the Java programming language. The communication between the different SCS components is done with Java Remote Method Invocation (RMI).

## III. THE XENON10 SHIELD

The XENON10 detector is protected from external background by a cubic steel-framed structure, consisting of 20 cm high-density polyethylene (HDPE) inside of 20 cm Pb; a schematic is shown in Fig. 12. The Pb was supplied in  $5 \times 10 \times 20$  cm bricks and was stacked so as to avoid any line-of-sight penetration along the cracks. The outer 15 cm of Pb have an activity in  $^{210}\text{Pb}$  of about  $560 \pm 90$  Bq/kg, while the inner 5 cm are a low-background Pb obtained from *Fonderies de Gentilly* [37]. It was measured at a germanium counting facility [32, 33] to have an activity in  $^{210}\text{Pb}$  of  $(17 \pm 5)$  Bq/kg. Specific activities for various shield components are shown in Table I.

A Monte Carlo simulation shows that 20 cm Pb results in an attenuation of the external gamma flux larger than  $10^5$  while its internal activity leads to a contribution of less than 0.32 cts/keVee/kg/day (dru) ( $E < 25$  keVee) to the raw event rate inside the shield cavity. With the additional self-shielding of the outer 2 cm of Xe (as used in the WIMP search data analysis [11]), the contribution of the Pb activity to the electron recoil background drops

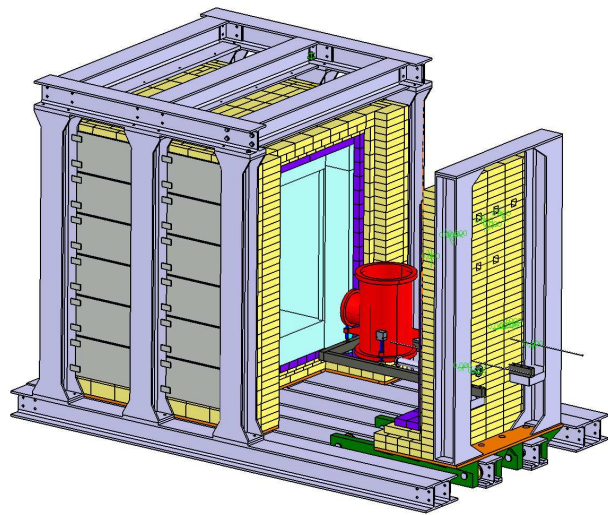


FIG. 12: (Color online) The XENON10 shield structure. Common and low-radioactivity Pb bricks are shown in yellow and purple respectively, while polyethylene is light blue. Not shown are the 20cm of polyethylene on the "door" and the 15cm below the shield structure.

below 0.05 dru ( $E < 25$  keVee), becoming sub-dominant (see Fig. 13).

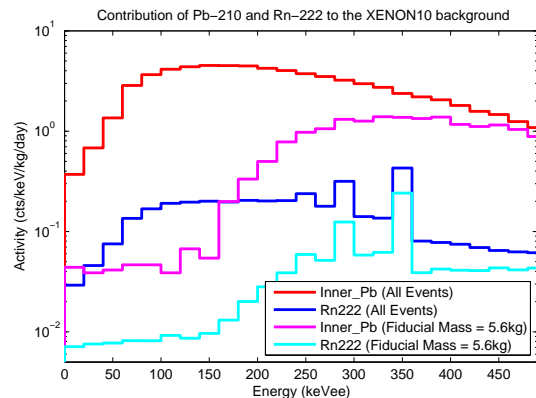


FIG. 13: (Color online) Simulated contributions of  $^{210}\text{Pb}$  (17 Bq/kg) and  $^{222}\text{Rn}$  (5 Bq/m<sup>3</sup>) to the XENON10 background, for the entire 14 kg active volume (red, blue) and also for a 5.6 kg fiducial volume (cyan, magenta); the fiducial volume corresponds to 2 cm Xe self-shielding (radial) and 3 cm each (Top/Bottom).

The 20 cm of HDPE provides reduction of external fast-neutron flux by a factor of 90. Placing the Pb outside the HDPE has the benefit that the neutron scattering on the Pb reduces the energy of the neutrons, thus increasing the efficacy of the HDPE. The dominant source of neutrons is expected from  $(\alpha, n)$  and fission reactions in the surrounding rock, as well as from cosmogenic production in the rock and Pb. The ambient neutron flux from natural radioactivity in the rock has been measured to be about  $4 \times 10^{-6}$  n/cm<sup>2</sup>/s [38, 39], and from this the in-



tegrated rate of neutron interactions in XENON10 is calculated to be  $< 0.015$  neutron/month in the dark matter region of interest. The muon flux in the cavern was measured to be  $1.06 \pm 0.03$  muon /m<sup>2</sup>/hour [40]; from this, and the muon-induced neutron yield in rock and in Pb, the expected rate for cosmogenic neutrons is expected to be about 13 times higher [41] than from natural radioactivity.

The internal shield cavity is  $107.5 \times 90 \times 90$  cm, of which the detector occupies about 30% of the volume. Care was taken not to leave any trapped air pockets between the lead and polyethylene, or anywhere else in the structure. An additional 15 cm HDPE is also present below the shield structure. All seams were coated with a low-radioactivity silicon-gel, and a 10 mm thick rubber seal runs in a 5 mm deep trench along the perimeter of the polyethylene on the door; thus the cavity is able to sustain a slight over-pressure, and boil-off N<sub>2</sub> from a low-pressure dewar is passed continuously into the top of the cavity at a rate of  $1.5 \pm 0.1$  standard liter/min, and allowed to exit at the bottom. The concentration of <sup>222</sup>Rn in the shield cavity, typically about 130 Bq/m<sup>3</sup>, was reduced by the N<sub>2</sub> purge to a value of  $< 5.5$  Bq/m<sup>3</sup> (consistent with the sensitivity floor of the RAD-7 radon measuring device [42]). The purge process occurred in about 30 hours. The expected contribution to the electron recoil background ( $E < 25$  keVee) from this level of Rn activity is  $7 \times 10^{-3}$  dru in the inner fiducial volume (Fig. 13).

The shield structure is secured by steel panels along the outer walls, with bolts passing through the HDPE sheets. The XENON10 detector is supported by stainless steel I-beams on a single wall, which also serves as a door and can be moved laterally on rails. All cryogenic and electronic feed-throughs pass through this wall, using a Z-shape where possible, and as far off-center as possible, to minimize line-of-sight. The overall diameter of each opening was also minimized, and gaps in the Pb (after placing the cables) were filled with low-radioactivity Pb shavings. Silicon-gel was used to fill holes in the HDPE, also ensuring air-tightness in these locations. During the construction all components were cleaned and prepped with Ethanol before mounting them on the shield structure. no cables or pipes have to be disconnected when opening the door to access the cryostat.

#### IV. THE XENON10 DATA ACQUISITION SYSTEM

To maximize the information available from time structure and amplitude of the primary (S1) and secondary (S2) pulses, the signal from 89 PMTs are individually digitized by an ADC array at 105 MHz (about 10 ns/sample). The S1 pulses from the direct scintillation light of a typical background event in the energy region of interest have 4-27 p.e. distributed over a width of  $< 200$  ns (with a characteristic decay time of  $\sim 27$  ns [43]).

The S2 pulses from the secondary proportional scintillation have  $\times 200$  the number of photoelectrons distributed over about 1  $\mu$ s. The distance between the S1 pulse and the S2 pulse vary from 0 to 80  $\mu$ s, the maximum drift time for electrons extracted in the liquid. Events with multiple scatters in the active Xe volume will have more than one S2 pulse. To guarantee that the S1 pulse and all S2 pulses associated with an event are digitized, a full waveform of 160  $\mu$ s is recorded for each event.

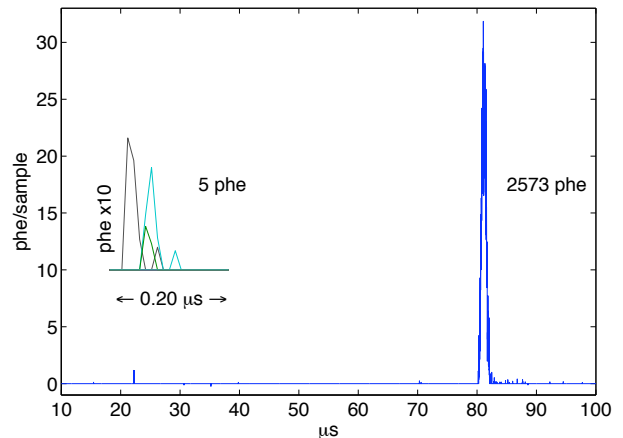


FIG. 14: (Color online) S1 and S2 pulses for 2.3 keVee gamma event in XENON10 background data. Signals from each PMT hit are plotted separately. An enlarged view of the S1 pulse (5 p.e.) is also shown. See [40] for more details.

The digitizers are *Struck 3301* fast ADC (VME bus) modules [44], with sampling frequency 105 MHz and 14-bit ADC resolution ( $+0.1$  V  $\rightarrow$   $-1.9$  V). The signal from each PMT is amplified using Phillips PS776  $\times 10$  amplifiers, and a single-pole RC filter (30 MHz) at the input to the ADC prevents aliasing. The filter also has a slight shaping effect; because a single photo-electron pulse width is similar to the inverse sample rate of the digitizer, this improves the single photoelectron sensitivity (see Fig. 14). An on-line software baseline-flattening algorithm sets small fluctuations in the baseline ( $< \pm 8$  digitizer bins) to zero, allowing for very efficient lossless data compression by a factor of  $\sim 20$  using open source software (gzip). The data is not further modified or processed before being recorded to disk.

The sum of the 30 central PMTs of the top array provides the global S2-sensitive event trigger (see Fig. 15). The summed signal is amplified  $\times 10$  by a CAEN N968 with integration time constant 1  $\mu$ s; this value was selected based on the width of the S2 signal. The shaped signal is then passed to a CAEN voltage discriminator. The S2 trigger was verified to have 100% efficiency for a square pulse voltage input of width 1  $\mu$ s and a step size 16 mV. Since a typical photoelectron from a PMT with  $2 \times 10^6$  gain has an integrated area of 16 mV $\cdot$ ns, this is equivalent to 100 photoelectrons. Considering that about 55% of S2 scintillation is recorded by the top PMT array, it is inferred that the trigger efficiency is 100% for

TABLE I: Results from radioactive measurements for relevant shield components (values in mBq/kg).

	$^{238}\text{U}$	$^{232}\text{Th}$	$^{210}\text{Pb}$	$^{235}\text{U}$	$^{40}\text{K}$	$^{137}\text{Cs}$	$^{60}\text{Co}$	$^{54}\text{Mn}$
Pb (inner)	< 3.9	< 6.8	$(17 \pm 5) \times 10^3$	< 20	< 28	< 0.85	< 0.19	
Pb (outer)	< 1.6	< 5.7	$(560 \pm 90) \times 10^3$	< 51	$14 \pm 6$	< 2.1	< 1.1	
Polyethylene	< 5.2	< 6.6		< 3.2	< 64	< 2.6		
Steel (I-beams)	$7.8 \pm 3.2$	< 4.1		< 3.1	< 15	< 1.4	$170 \pm 3$	$3.3 \pm 0.6$
Steel (side panels)	< 3.5	< 4.7		< 1.8	< 26	< 2.2	$2.4 \pm 0.7$	
Steel (ceiling plate)	< 8.3	< 8.7		< 5.7	< 42	< 2.8	$2.9 \pm 1.2$	$2.0 \pm 0.8$

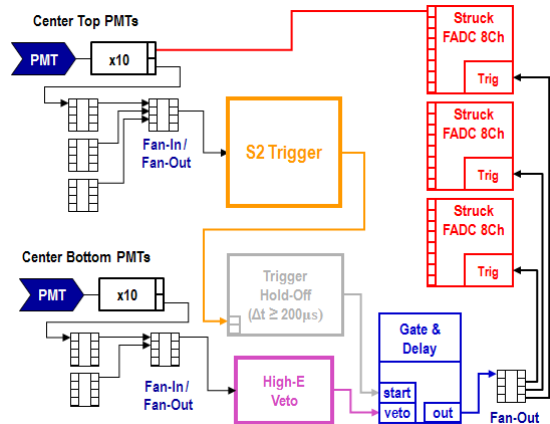


FIG. 15: (Color online) Schematics for the XENON10 Data Acquisition System electronics.

S2 events of 182 phe or greater. Because a single ionized electron extracted from LXe typically yields  $24 \pm 5$  photoelectrons (after taking into account light collection and PMTs quantum efficiency), 182 photoelectrons in the S2 signal corresponds to 7 – 8 ionized electrons. This is the expected charge from an event with about 1 keV nuclear recoil equivalent energy [4]. The trigger signal is distributed from the discriminator to all ADC modules simultaneously using a Fan-Out chain. The S2 trigger provides a lower threshold than is possible with an S1-based trigger (as is evident from Fig. 14); moreover, an S2-trigger allows for elimination of S1-only events due to scatters in the charge-insensitive regions of the detector, thus reducing the trigger rate. A trigger hold-off is used to prevent the system from triggering on after-pulsing following a large S2 pulse. The hold-off requires that no S2 trigger candidates occur for the previous 200  $\mu\text{s}$  before allowing a trigger to start acquisition. The hold-off time is included in computing the acquisition dead time. For gamma calibration data runs, a high energy S1 veto is added to reduce the trigger rate. The veto is based on the sum of the 9 center bottom array PMTs and eliminates events with an  $\text{S1} > 150$  keVee. Using the S2-trigger and no high energy veto, the acquisition rate during WIMP search mode is  $\sim 2.5$  Hz, leading to a dead time of 7%.

## V. THE XENON10 DATA PROCESSING AND ANALYSIS

### A. S1 & S2 Pulse Identification

The raw data for an event consist of 88 waveforms of 16350 samples and is reduced to physical parameters using two fully separate and parallel analysis chains. One is written in ROOT [45], and the other uses the commercial MATLAB software; both were specifically developed for the XENON10 data analysis. The high-level structure of the data reduction is similar in both cases, and proceeds in three stages: i) preprocessing the waveforms, ii) searching for pulses, and finally iii) computing the reduced quantities associated with each scintillation pulse.

In the preprocessing stage, the samples of each PMT waveform are zeroed if they are below a threshold of  $\sim 1$  mV, which is much lower than the single photoelectron level and which depends on the noise characteristics of the channel. The waveforms of all channels are then added into a total waveform that is used to search for S1 and S2 pulses.

The pulse searching stage operates in two steps: it first looks for S2-like pulses in the entire waveform and then looks for S1-like pulses that precede the first S2-like pulse. Fig. 16 shows a typical events with S1 and S2 and their hit patterns on the PMTs.

The S2 pulse finding algorithm starts by applying a digital filter to the entire waveform to smooth out the high frequency components in order to facilitate the detection of the extent of pulses. It then searches the filtered waveform for regions where the signal exceeds a threshold of 10 mV for at least  $0.6 \mu\text{s}$ , a time interval large enough to contain at least one S2 pulse, and for which the preceding and following  $0.2 \mu\text{s}$  have an average signal less than 5% of the maximum within the interval. Because of the long afterpulsing tails that follow large S2 pulses the interval above threshold will often contain multiple pulses. The algorithm then recursively searches for S2 like pulses within that interval. This is done by computing the extent of any potential pulse by starting from its maximum sample in the interval and going backward in the trace until either the signal drops below 0.1% of its maximum or the slope of the signal changes sign. This defines the left boundary of this pulse. The same procedure is repeated going forward in the trace to find the right boundary. If the pulse found has a FWHM larger

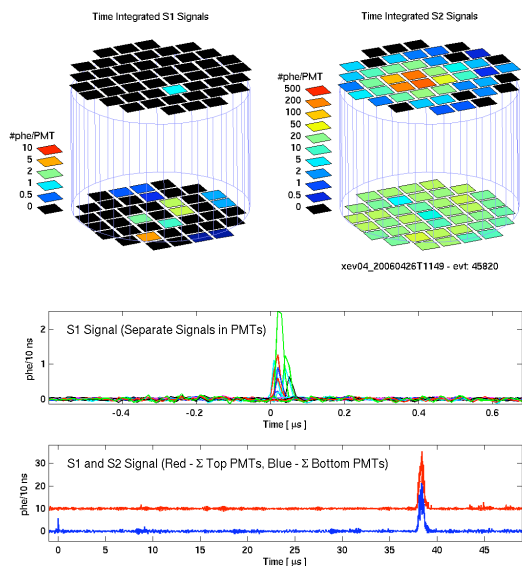


FIG. 16: (Color online) A typical event showing  $S1$  and  $S2$  and their hit patterns on the two arrays of PMTs (from [41])

than  $0.4 \mu\text{s}$  it will be considered as an  $S2$  pulse and its location and boundaries will be saved. The recursive search for  $S2$  pulses then continues within the interval (excluding the regions where any pulse might already have been found). The parameters of the four largest  $S2$  pulses are kept. A key difference in the MATLAB-based analysis was the development of a custom double box filter [46], with the width of the two boxes set to 10 and 100 digitizer samples, respectively. These choices correspond to the approximate width of  $S1$  and  $S2$  signals. This filter proved extremely adept at correctly identifying the smallest  $S2$  pulses.

The  $S1$  pulse finding algorithm searches the total waveform for signal excursions of at least 12 mV above the baseline. The boundaries of the potential pulse are defined as the points where the signal drops below 0.1% of its maximum. If the  $0.5 \mu\text{s}$  preceding the pulse and the 50 ns following the pulse respectively have an average signal less than 0.5% and 4% of the maximum, and if the decay time of the pulse is faster than 200 ns, then its location and boundaries will be saved. The parameters of the two largest  $S1$  pulses identified are kept.

Once all the pulses have been identified, the reduction enters its last stage, computing the quantities of interest. Each PMT waveform is integrated over the boundaries of the  $S1$  and  $S2$  pulses identified and the values are converted into photoelectrons using the PMT gains. For each pulse a number of quantities are computed: FWHM, height, mean arrival time, number of PMT coincidences, number of digitizer channels saturating, etc. The  $XY$  position of each  $S2$  pulse is computed using two different position reconstruction techniques (see section VB). A few parameters of the entire waveform are also com-

puted: its total area, the average and RMS of the baseline before any pulses, and finally the total  $S1$  and  $S2$  signals.

## B. Event Position Reconstruction

An important feature of the XENON10 detector is its ability to localize events in 3D, enabling background reduction with fiducial volume cuts and multiple scatter events rejection. Due to the small spread of the drifting electrons by diffusion in LXe [47], the proportional scintillation signal is localized to a region with the same  $XY$  coordinates of the interaction site. Near the edge of the TPC, field non-uniformities lead to systematic radial displacements towards the center of about 1 mm. Charge focussing effects in the extraction region between gate mesh and anode lead to charge displacements of less than half the mesh pitch, i.e.,  $< 1$  mm. The event  $z$ -coordinate, along the electric field direction, is inferred from the time difference between the primary and secondary signals, with a resolution which is  $< 1$  mm given the precision of the time measurement. Events with energy depositions at different  $z$  positions will produce more than one  $S2$  signal and can thus be readily identified and rejected.

To obtain the  $XY$  event localization, with a few mm resolution, much smaller than the dimension of the PMTs, the light pattern measured by the top PMT array must be de-convolved. Two light pattern recognition algorithms were developed and tested on XENON10 data: a minimum  $\chi^2$  algorithm and a neural network ( $NN$ ) based algorithm.

The minimum  $\chi^2$  algorithm compares the measured light pattern with simulated  $S2$  signals, calculating the values

$$\chi^2(x, y) = \sum_{i=1}^M \frac{[S_i - s_i(x, y)]^2}{\sigma_i^2} \quad (2)$$

for all simulated  $XY$  positions. In this formula  $S_i$  and  $s_i$  are the measured and simulated  $S2$  signals (in numbers of photoelectrons) on the  $i$ -th PMT,  $M$  is the total number of PMTs (48 in the top array), and  $\sigma_i$  takes into account the uncertainties of both the measured and simulated signals. The minimum value of the  $\chi^2(x, y)$  function is used as an estimator for the true position in the  $XY$  plane. If the statistical uncertainty in the simulated  $S2$  pattern is small, the main contribution to  $\sigma_i$  is the fluctuation in the measured signal, which includes the statistical fluctuation on the photoelectric emission from the PMT photocathode  $\sigma_{pe,i}$  and the fluctuation  $\sigma_{g_i}$  on the gain  $g_i$ . If the number of detected photoelectrons is sufficiently large,  $\sigma_{pe,i}$  can be approximated as  $\sigma_{pe,i} \cong \sqrt{S_i}$  while  $\sigma_{g_i}$  is measured for each PMT through its single photoelectron spectrum

$$\sigma_i^2 = \sigma_{pe,i}^2 \left[ 1 + \left( \frac{\sigma_{g_i}}{g_i} \right)^2 \right] = S_i \left[ 1 + \left( \frac{\sigma_{g_i}}{g_i} \right)^2 \right] \quad (3)$$

The second algorithm is based on a fast artificial neural network. Its adaptive properties enable estimation of the vertex position even with a degraded input pattern, e.g., due to non-functioning PMT channels. The speed of the algorithm is nearly independent of the dimension of the detector.

Due to the cylindrical geometry of the active volume, we chose an algorithm based on two different sub-networks, working simultaneously to estimate the polar coordinates, radius  $r$  and polar angle  $\theta$ . The NNs are feed-forward multilayer perceptrons with two hidden layers. We applied an hyperbolic tangent as activation function for the neurons in the hidden layers, with linear output for the output neuron. The network was trained, using the backpropagation rule, on a set of  $4 \times 10^4$  simulated events, with the same simulation code used for the  $\chi^2$  algorithm. The events were randomly generated in the  $XY$  plane with a mean value of  $2.5 \times 10^3$  pe/events. This number is sufficiently large to minimize statistical fluctuations in the total number of detected photoelectrons, and is comparable to the typical S2 signals in the energy range of interest.

The input for both NNs is a vector with the top PMT signals in number of photoelectrons, normalized by the sum of their signals. In this way the output of the NNs is almost independent of signal size. The MC-estimated error on the radial position  $r$  is  $\sim 0.7$  mm for  $r < 80$  mm, and rises to 1.2 mm near the edge of the active volume. Fig. 17 shows a map of the reconstructed interaction vertices produced by a Cs source placed near the cryostat. The source location is apparent. In fig. 18 the radial distributions of the Cs-interaction vertices obtained through NNs and  $\chi^2$  reconstruction algorithms are compared with the corresponding MC simulation. Clearly the NN distribution is in better agreement with the MC simulation near the edge of the detector, where reflection of scintillation light on the Teflon renders the vertex reconstruction more difficult. Both NN and  $\chi^2$  distributions show very good agreement with the simulated data for  $r < 80$  mm.

### C. Basic Quality Cuts

A number of basic quality cuts were defined to remove events that do not correspond to real energy depositions in the detector, events with unphysical parameters, events with misidentified features, etc.. Many of the basic quality cuts are based on the known physical properties of the direct scintillation light of LXe and on the characteristics of proportional scintillation of gaseous Xe.

The basic quality cuts applied to the S1 signal are on the number of PMT coincidences, on the width and on the mean arrival time. In order to clearly distinguish low energy S1 signals from random single photoelectrons, the minimum coincidence requirement is set to 2 PMTs having a signal above 0.35 pe. The efficiency of this cut is shown in figure 19. In addition, the width at 50% height

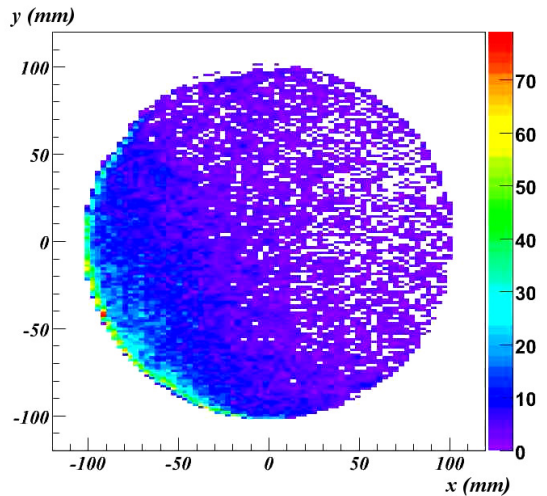


FIG. 17: (Color online)  $XY$  map of the reconstructed vertices with an external  $^{137}\text{Cs}$  source: the position of the source can be clearly inferred.

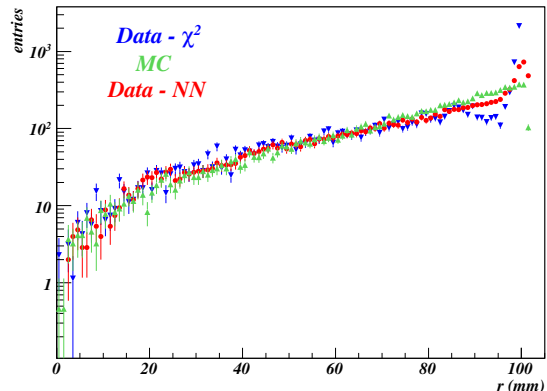


FIG. 18: (Color online) Data-MC comparison between the radial distribution of the vertices in the case of a  $^{137}\text{Cs}$  source irradiation of XENON10: the MC distribution (green) is plotted with the real data distributions obtained through NN (red) and  $\chi^2$  (blue).

of the S1 pulse is required to be larger than 20 ns and smaller than 150 ns (note that this is the width in the digitized trace, after the anti-aliasing filter of the FADC as described in section IV) and its mean arrival time is required to be shorter than 60 ns. These cuts ensure that the S1 signal is not confused with noise or with small single electron S2 signals, for example.

Multiple basic quality cuts are also applied to the S2 signal. They consist of a cut to reject events with more than one S2 pulse, a cut on the width, a cut to remove events with ADC saturation and a cut on the proportion of the S2 signal seen by the top and bottom PMT ar-

rays. As WIMPs are not expected to scatter more than once in the detector, events with more than one S2 pulse are usually discarded. This is also necessary for other analyses, when looking at the spatial dependence of the direct scintillation for example (section VIA 3). In terms of pulse shape, the FWHM of the S2 signal is required to be larger than  $0.5 \mu\text{s}$  but less than  $1 \mu\text{s}$ , consistent with what is expected from the proportional scintillation gap. Events for which the S2 signal peaks at a higher voltage than the input range of the FADC are also removed, although this effect is absent at energies lower than 50 keV. Monte Carlo simulations have shown that the expected fraction of S2 light measured by the top (bottom) PMT array should be about 55% (45%) and is consistent with what is observed in calibration data. Consequently, events where the ratio of S2 light seen on the top and bottom arrays falls outside the expected range are also rejected. For example, very large S1 signals from alpha particles misidentified as S2 pulses would be cut since the bottom array would measure a much larger proportion of the signal.

Another cut, intended to remove events in which the XY position has been incorrectly inferred, is also applied. The cut requires the  $\chi^2$  between the S2 signal distribution from data and the Monte Carlo simulated distribution at the position inferred from the Neural Network algorithm to be less than a threshold value.

Finally, an additional important parameter, related to the quality check of the pulse finding algorithm, is defined as

$$\log \left( \frac{S1 + S2}{A - S1 - S2} \right) \quad (4)$$

where  $A$  is the total area of the trace and  $S1$  and  $S2$  are the total signals identified. This parameter is analogous to a signal to noise ratio since it will be very large when all the features of the waveform have been identified and are included in the total  $S1$  and  $S2$  signals whereas it will be very low if some features have been not been identified.

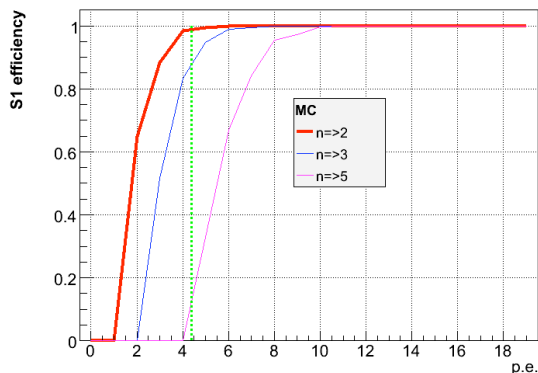


FIG. 19: (Color online) Probability of S1 identification as a function of the number of required coincidences.

## VI. THE XENON10 CALIBRATION DATA RESULTS

### A. Gamma Calibration

To achieve a reliable and accurate detector calibration, with minimum impact on WIMP search exposure time, the XENON10 shield was designed to allow introduction of external calibration sources without exposing the detector cavity to outside air. The gamma calibration sources used were  $^{57}\text{Co}$ ,  $^{137}\text{Cs}$ ,  $^{60}\text{Co}$  and  $^{228}\text{Th}$ . The gamma source calibration data are used not only to determine the energy scale based on S1 (or S2) signals, but also to define the detector's response to electron recoils from background events.

#### 1. S1 light yield and energy scale

The direct scintillation (S1) light yield in XENON10 depends on the event energy and position as well as on the electric field strength in liquid xenon. The operating field in XENON10 was  $0.73 \text{ kV/cm}$ . Measurements of the S1 yield at this field were carried out with gamma sources. In the bulk region ( $r < 5 \text{ cm}$ ), the 662 keV photo-absorption peak of  $^{137}\text{Cs}$  gives an average light yield of  $2.2 \pm 0.1 \text{ p.e./keV}$ . For 122 keV gammas from  $^{57}\text{Co}$  source, the light yield is about  $3.1 \text{ p.e./keV}$ , for events with radial positions between 8 and 9 cm, as shown in Fig. 20. The different light yield for different gamma ray energies is due to the different contribution of the electron-ion recombination [28]. We were also able to observe the 30 keV characteristic X-ray peak for events near the edge of the sensitive volume.

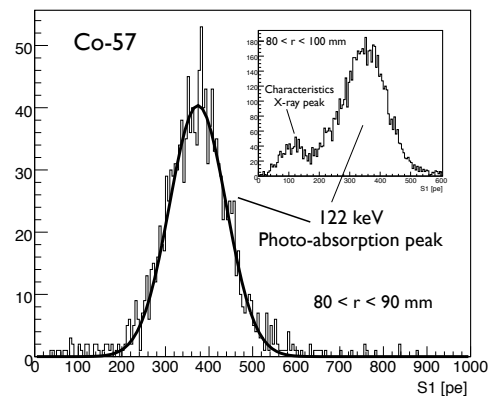


FIG. 20: S1 scintillation spectrum from  $^{57}\text{Co}$  gamma calibration.

## 2. S2 yield and liquid xenon purity

The proportional scintillation light S2 is proportional to the number of electrons liberated in the liquid by an ionizing event. The number of electrons which reach the liquid-gas interface depends strongly on the liquid xenon purity, which can be inferred from a measurement of the electron lifetime  $\tau$  [48]. The presence of impurities reduces the number of electrons produced in the liquid at time  $t=0$  ( $N_e(0)$ ) according to the relation:  $N_e(t) = N_e(0)e^{-t/\tau}$ . To determine the electron lifetime, we used the data from  $^{137}\text{Cs}$  calibration, measuring the attenuation with drift time of the S2 signal associated with the full energy peak of 662 keV gamma rays. Throughout the dark matter search period an electron lifetime longer than 2 ms was measured, corresponding to  $\ll 1$  ppb  $\text{O}_2$  equivalent impurity concentration in the LXe. A similar purity level was inferred during a subsequent calibration of XENON10 with gamma rays from neutron-activated Xe gas, carried out shortly after the first dark matter search run was completed. Fig. 21 shows the electron lifetime measurement using S2 from the 164 keV gamma events uniformly distributed in the XENON10 active volume. The electron lifetime inferred from this calibration is  $2.2 \pm 0.3$  ms, confirming the excellent purity level achieved in XENON10 during the dark matter search.

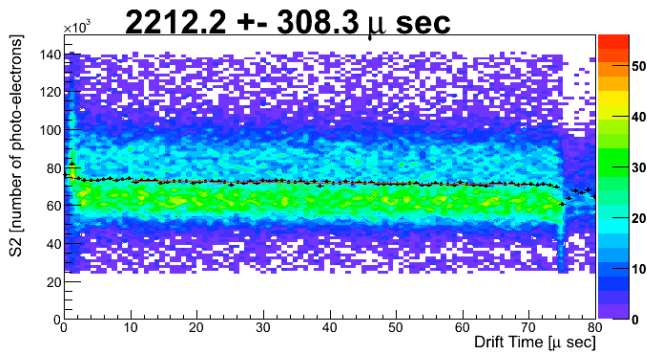


FIG. 21: (Color online) Determination of the electron lifetime from calibration data. The band is the S2 signal measured by the bottom PMT array as a function of drift time for fully-absorbed 164 keV gamma events from the activated Xe calibration of XENON10.

As previously discussed, the amplitude of the S2 signal, for a given number of ionization electrons extracted from the liquid, depends on several factors: the gas pressure  $p$ , the gas gap  $x$ , the electric field  $E$  across the gap, the light collection efficiency of the PMTs, and the quantum efficiency  $Q_E$  of the PMTs. The observed number of photoelectrons per electron drifting in the gas can be found from single electron pulses within the data. During the operation of the XENON10 detector, a class of pulses due to single electron emission from the liquid to the gas phase was observed (Fig. 22). From this observation, we estimate that, on average, each electron produces 13.8

p.e. on the top PMT array and 9.9 p.e. on the bottom PMT array respectively.

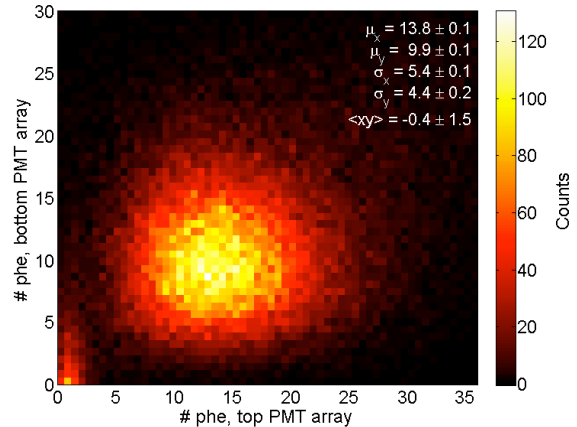


FIG. 22: (Color online) S2 from single electrons seen in the neutron calibration data, with the signal detected by the top PMT array on the x-axis, and bottom PMT array on the y-axis. These events were selected based only on pulse width (full width  $0.2 \mu\text{s} - 3.0 \mu\text{s}$ ) plus a requirement that they would be at least  $10 \mu\text{s}$  from the trigger region (either before or after).

## 3. Position-dependence of S1 and S2 Signals

The S1 light collection efficiency (LCE) has a strong dependence on the event position, due to the effects of total internal reflection at the liquid-gas interface, the solid angle, the optical transmission of the grids and the teflon reflectivity. In order to obtain an accurate energy calibration, data from both Monte Carlo simulation and internal sources were used to study the position dependence of the signals.

Fig. 23 shows the simulated S1 LCE throughout the XENON10 detector, where we define LCE as the probability of photons released in the detector to hit the photocathode of a PMT; it does not include the QE of the PMTs. Some regions are light- but not charge-sensitive, most notably in the reverse field region between cathode and bottom PMT array. Some light sensitivity also exists in the xenon around and below the bottom PMT array, where stray light enters through openings between the Teflon cylinder and the PMTs. The primary light is predominantly detected by the bottom PMT array, due to total internal reflection at the liquid-gas interface, where the index of refraction changes from 1.61 [49] to 1. The ratio of top to bottom S1 signal ranges from  $\sim 0.14$  to  $\sim 0.3$  from the bottom to the top of the drift region. Some light is absorbed by the meshes, by the PTFE walls, or by the liquid xenon. We calculated 92% transparency of the meshes and assumed 92% reflectivity for PTFE [28]. The absorption length of liquid xenon is taken as 100 cm and the scattering length as 30 cm [50].

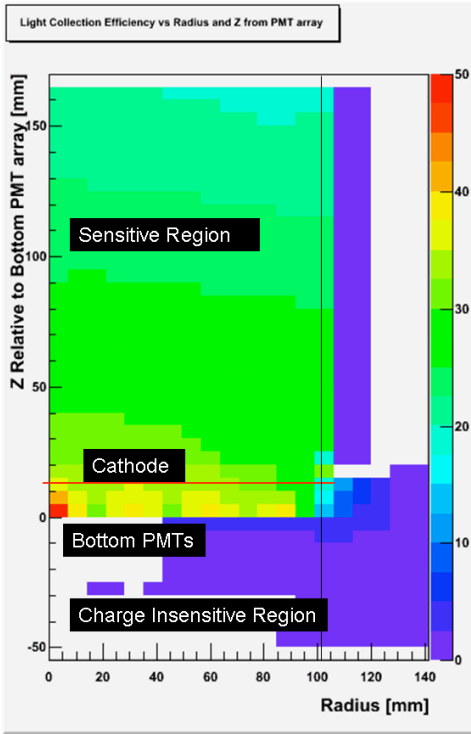


FIG. 23: (Color online) Simulated S1 light collection efficiency throughout the XENON10 detector.

In addition to the simulations, we also used neutron activated xenon isotopes, primarily  $^{131\text{m}}\text{Xe}$  (164 keV gammas) and  $^{129\text{m}}\text{Xe}$  (236 keV gammas) to calibrate the detector's S1 response throughout the entire active volume. The activated xenon isotopes were introduced into the XENON10 detector following several days of neutron activation of natural xenon [51]. Unlike external calibration sources, activated Xe isotopes provided unique energy and position calibration throughout the entire LXe sensitive volume. The excellent 3D position sensitivity of XENON10 allows event-by-event signal correction based on position. Fig 24 shows the S1 light yield for 164 keV gamma rays throughout the sensitive volume. The data can be compared with the simulated S1 response (Fig. 23) to determine parameters such as PTFE reflectivity and liquid xenon absorption length, that is relevant for the light collection. The response of the S2 signal at different  $XY$  positions was also studied using the 164 keV gamma calibration data (Fig. 25). The signal size differs by about 50% from the edge to the center, due to the sagging of the meshes which changes the gap where proportional scintillation light is generated.

We used the S1 and S2 light response maps from activated Xe calibration as a function of event position to correct the signals in the final data analysis. Better energy scale, electron/nuclear recoil discrimination and better energy resolutions were achieved after the position-dependent corrections of the two signals.

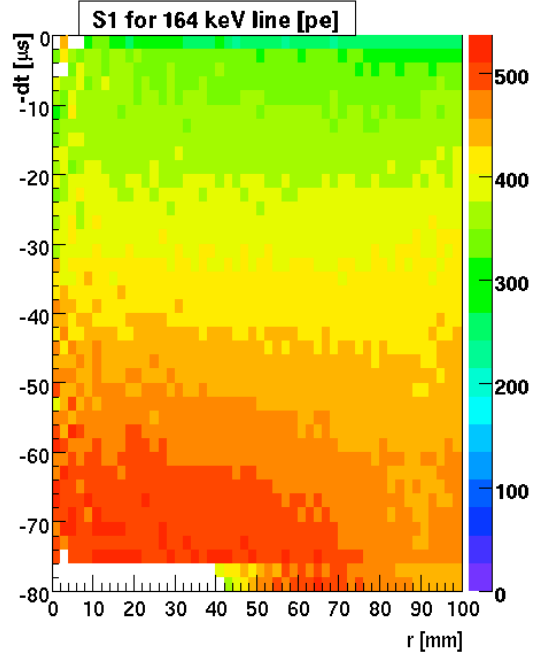


FIG. 24: (Color online) S1 light yield throughout the sensitive liquid xenon target from activated xenon calibration with 164 keV gamma rays.

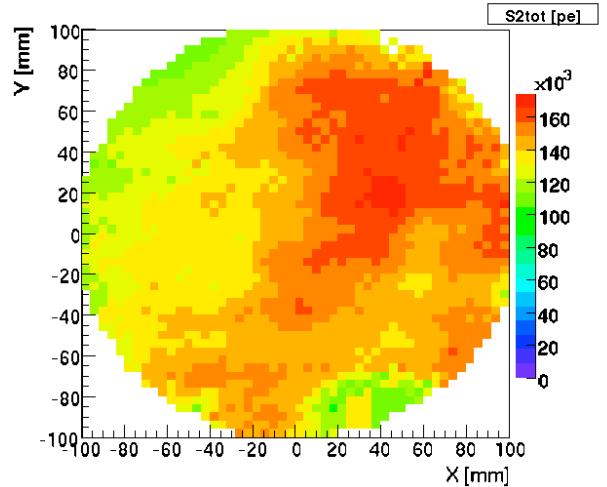


FIG. 25: (Color online) S2 light yield response at different  $XY$  positions from activated xenon calibration with 164 keV gamma rays.

#### 4. Combined energy scale

A recombination-independent combined energy scale for electron recoils, as described in details in [52, 53], can be produced from the appropriate sum of light (S1) and charge (S2). This scale should be free of the nonlinearities

present in the  $S1$ -based scale. The energy deposited by each event is determined by combining  $S1$  and  $S2$  signals as following,

$$E = \left( \frac{S1}{\alpha} + \frac{S2}{\beta} \right) \cdot W_{tot} \quad (5)$$

where  $S1$  and  $S2$  are in units of number of photoelectrons ( $N_{pe}$ ).  $\alpha$  and  $\beta$  are experimentally determined parameters in units of  $N_{pe}/\text{photon}$  and  $N_{pe}/\text{electron}$ , respectively.  $W_{tot}$  is the average energy required to produce either a scintillation photon or an ionization electron in LXe. In XENON10,  $\beta$  is determined from the  $S2$  corresponding to the single-electron emission peak (see Fig. 22). The anti-correlation between  $S1$  and  $S2$  is due to electron-ion recombination fluctuation in LXe. Each recombined electron-ion pair will create one UV photon. Thus,  $\alpha$  in equation 5 can be determined by  $\beta$  and the slope  $\theta$  in Fig. 26, according to the relation  $\alpha = \beta / \tan \theta$ . From the 164 keV calibration peak, we obtain,

$$W_{tot} = 14.0 \text{ eV} \quad (6)$$

in good agreement with a study in a small LXe detector [54]. The energy resolution of the XENON10 detector was investigated with gamma ray sources ( $^{57}\text{Co}$ ,  $^{22}\text{Na}$ ,  $^{137}\text{Cs}$ ,  $^{228}\text{Th}$ ) covering the energy range between 122 keV to 2.6 MeV. An example, from  $^{137}\text{Cs}$  662 keV gamma rays, is shown in Fig 27. For comparison, we also plot the energy resolution, in Fig. 28, obtained by using only  $S1$ , only  $S2$  and the sum of these two signals. At 1 MeV, the resolution from the combined energy measurement is about a factor of seven better than that from  $S1$  alone, and a factor of three better than that from  $S2$  alone. The energy determined from the combination of  $S1$  and  $S2$  signals show a much more linear response than that based on  $S1$  or  $S2$  alone (see Fig. 29).

## B. Neutron Calibration

To understand the XENON10 response to nuclear recoils, a neutron calibration was performed using a 3.7 MBq  $^{241}\text{AmBe}$  source, emitting  $\sim 220$  neutrons/second. The calibration was done by exposing the XENON10 detector to the source for approximately 12 hours, with a live time fraction of 0.92. The  $^{241}\text{AmBe}$  source (attached to a steel rod) was inserted through a 7 mm diameter hole in the XENON10 shield. The source was positioned next to the cryostat, between two 5 cm thick Pb bricks used to block high energy (a few MeV) gamma rays produced by the source.

The emitted neutrons have energies ranging from 0.1 MeV to 11 MeV, with a mean at 4.3 MeV. The calibration data were recorded at a constant rate of 6.5 Hz during the exposure. The trigger setup was the same as used for the WIMP search, with the addition of a high energy veto to reject events with energies above  $\sim 120$  keV.

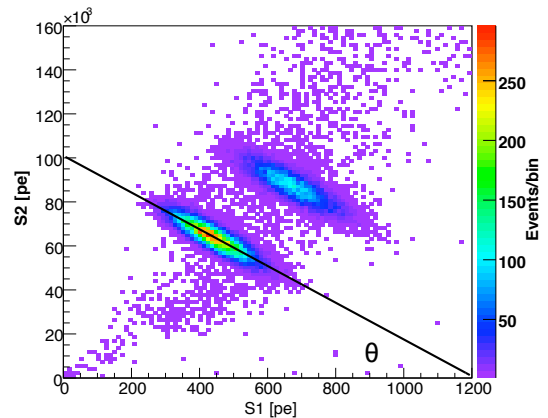


FIG. 26: (Color online) Anticorrelation between  $S1$  and  $S2$  for 164 keV and 236 keV  $\gamma$  rays from activated xenon isotopes ( $^{131\text{m}}\text{Xe}$  and  $^{129\text{m}}\text{Xe}$ ).

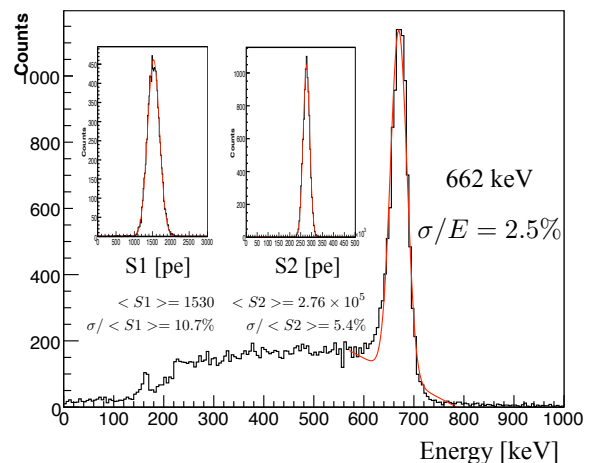


FIG. 27: Combined energy spectrum for single-scatter events from 662 keV gamma rays interacting within the 5.4-kg fiducial mass of XENON10. Insets:  $S1$  and  $S2$  distributions for 662 keV photo-absorbed events (events within  $2\text{-}\sigma$  around the 662 keV peak in the combined energy are selected). The energy resolution at 662 keV is 10.7%, 5.4% and 2.5% for  $S1$ ,  $S2$  and the combined energy, respectively.

Figure 30 shows the  $\log_{10}(S2/S1)$  vs.  $S1$  distribution from the neutron calibration run, after applying the quality cuts discussed in Section V C. Two regions are clearly distinguished in Figure 30: region a) which defines the nuclear recoil band corresponding to single elastic scatters, and region b) which corresponds to inelastic neutron scatters with  $^{129}\text{Xe}$ , which produce 40 keV gamma rays. Neutron inelastic scatters with  $^{131}\text{Xe}$  will produce 80 keV gamma rays, however the data do not show a peak around this value because of the events rejection by the high energy veto. The nuclear recoil band is used to determine XENON10 discrimination power, described in Section VI C.



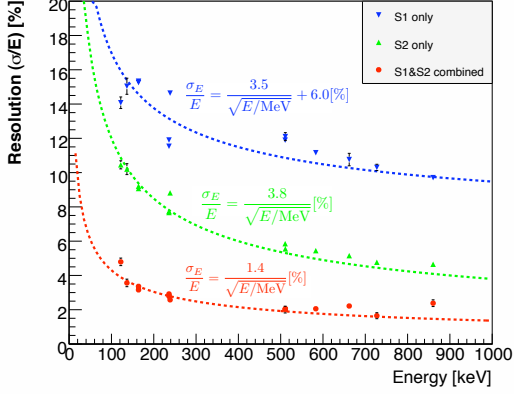


FIG. 28: (Color online) Energy dependence of resolutions in liquid xenon for  $S1$  (scintillation) only,  $S2$  (ionization) only and combined (scintillation plus ionization) energy spectra, obtained for gamma rays below 1 MeV in XENON10.

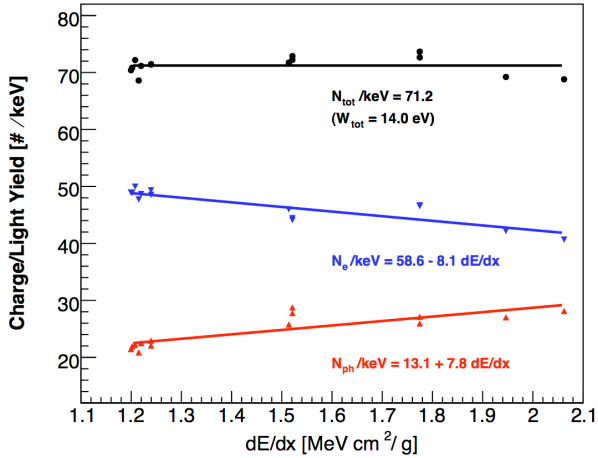


FIG. 29: (Color online) Number of scintillation photons ( $N_{ph}$ ) and ionization electrons ( $N_e$ ) per unit energy from gamma rays interaction in liquid xenon via photo-absorption for different stopping power ( $dE/dx$ ) at the operating field (0.73 kV/cm) of XENON10. Values of  $dE/dx$  corresponding to different energy of electrons (from photo-absorption of gamma rays) can be obtained from the ESTAR database [55]. The total number of quanta (photons plus electrons) per unit energy does not depend on the energy of gamma rays.

### C. Nuclear/Electron Recoil Discrimination

The success of XENON10 as a dark matter detector hinges in large part upon its ability to discriminate electronic recoils from nuclear recoils, which in turn requires adequate definition of the detector response to such events based on calibration data. In addition to the formation of excitons, recoiling particles will produce a population of ionized electrons, many of which promptly recombine with their parent ions. Under an applied elec-

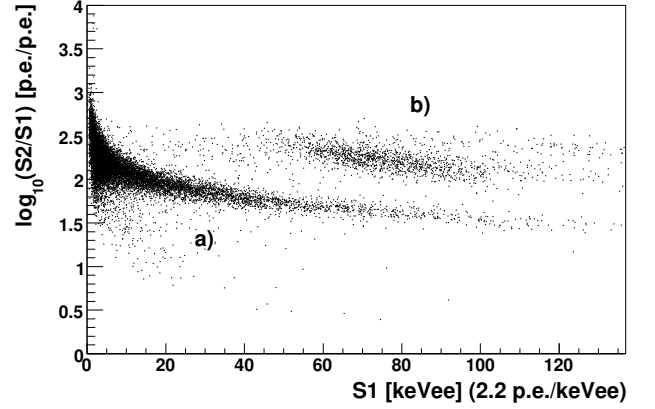


FIG. 30:  $\log_{10}(S2/S1)$  vs.  $S1$  distribution from neutron interactions in the XENON10 detector. The data show two different regions: region a) which corresponds to recoils from elastic scatters and defines the nuclear recoil band, and region b) which corresponds to recoils from inelastic scatters.

tric field, the relative number of recombining electrons decreases. However, because nuclear recoils have a characteristically higher ionization density than electronic recoils, fewer electrons escape recombination from recoiling nuclei than electrons, for a given energy and drift field.

Electrons which recombine contribute to the prompt scintillation signal ( $S1$ ), while those which escape recombination are drifted to the anode in the gas and produce the proportional signal ( $S2$ ). The relative strength of recombination for a given event can be measured by the ratio  $S2/S1$ , and hence this parameter can be used to discriminate between recoiling species. Figure 31 shows the behavior of  $\text{Log}_{10}(S2/S1)$  as a function of energy, in unit of keV electron-equivalent (keVee), for populations of both recoil types, called the electronic and nuclear recoil bands, or ER and NR bands, respectively. The main purpose of such ER and NR calibrations is to identify a region in  $\text{Log}_{10}(S2/S1)$  vs.  $S1$  space, called the WIMP acceptance window, which should be nearly free of ER events while covering a significant portion of the NR band. The lower bound of this window along the horizontal axis is determined by the detector's  $S1$  threshold, and the corresponding upper bound is chosen to maximize the potential integrated WIMP rate while minimizing the effects of anomalous background events which occur mostly at higher energies (see section VII B). The choice of bounds along the vertical axis are discussed here.

Data were taken with the  $^{137}\text{Cs}$  source throughout all of November 2006, and intermittently from December 1 through February 14, 2007, accumulating a total of  $\sim 2100$  events (after quality and fiducial cuts) in the WIMP acceptance energy window,  $4.4 \text{ p.e.} < S1 < 26.4 \text{ p.e.}$ . Fluctuations in  $\text{Log}_{10}(S2/S1)$  over most of

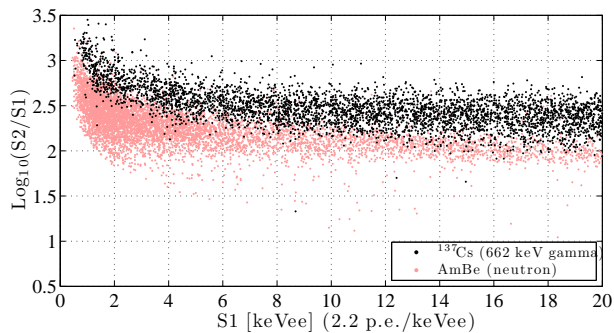


FIG. 31: (Color online) The electronic and nuclear recoil bands shown in  $\text{Log}_{10}(S2/S1)$  vs.  $S1$  space.

this range are dominated by recombination fluctuations, until the lowest energies where uncorrelated statistical fluctuations take over. The width of the electronic recoil band is very important for gamma rejection because the two bands overlap. Due mainly to the non-uniform  $S1$  response at different locations in the fiducial region, applying spatially-dependent corrections to  $S1$  based on the  $^{131m}\text{Xe}$  calibration (see section VIA 3) improves the overall  $S1$  resolution and thus helps to reduce the variance of the bands. Data with the AmBe neutron source were taken on December 1, 2006 for approximately 12 hours, accumulating a total of about 260,000 events. The energy dependence of both bands makes it difficult to precisely measure the discrimination power in the absence of extraordinarily large calibration datasets. In an effort to remove this energy-dependence, a one-dimensional transformation that “flattens” the ER band is applied to all data. The ER band is broken up into 1 keVee-wide, vertical slices in  $S1$ . For each, a Gauss fit is applied to the  $\text{Log}_{10}(S2/S1)$  spectrum. The mean of each fit now represents the center of the ER band in that particular bin. A high-order polynomial is fit to the Gauss means, which provides an analytic form for the ER band centroid as a function of  $S1$ , and is subtracted from every data point in both bands. This procedure flattens the ER band (and to a large extent, the NR band as well), and introduces a new parameter,  $\Delta\text{Log}_{10}(S2/S1)$ , which represents the distance from the ER centroid in  $\text{Log}_{10}(S2/S1)$  space. Figure 32 shows the bands in  $\Delta\text{Log}_{10}(S2/S1)$  space.

Although the energy dependence of the ER band centroid has been removed, the NR band centroid and width still change with energy. Again, the flattened bands are broken up into vertical  $S1$  slices, only this time more coarse binning is used—seven bins in the WIMP energy region of interest (ROI)—in order to maximize the statistics in each slice, and a Gauss fit is applied to the  $\Delta\text{Log}_{10}(S2/S1)$  spectrum of both bands. One such slice is shown in Figure 33, for the range 13.4–17.2 keVr (1 keVr = 1.1 pe, according to [11]) of nuclear recoil energy. The WIMP acceptance window is defined to lie in the range  $(\mu - 3\sigma) < \Delta\text{Log}_{10}(S2/S1) < \mu$ , where  $\mu$  and  $\sigma$  are the

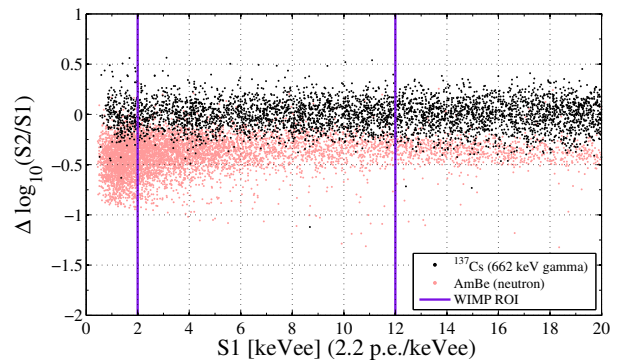


FIG. 32: (Color online) The bands in figure 31 have been transformed to show the distance in  $\text{Log}_{10}(S2/S1)$  space from the ER band center, giving the new discrimination parameter,  $\Delta\text{Log}_{10}(S2/S1)$ . The vertical lines indicate the WIMP region of interest (ROI).

mean and sigma from the NR band Gauss fits, respectively. The Gauss fits were performed only to define the window bounds; the NR acceptance,  $A_{nr}$ , was calculated by counting the number of AmBe events that fall within this window, for each energy bin.

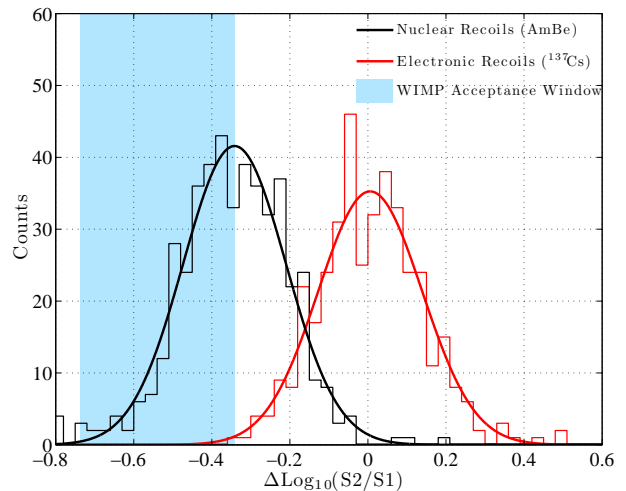


FIG. 33: (Color online) Distributions of  $\Delta\text{Log}_{10}(S2/S1)$  for nuclear and electronic recoils in the range 13.4–17.2 keVr. The WIMP acceptance window in this particular energy range is defined by the blue, shaded rectangle which is between  $\mu$  and  $\mu - 3\sigma$  of the NR band.

The shape of the  $\Delta\text{Log}_{10}(S2/S1)$  fluctuations in the ER band are “empirically” Gaussian; that is, with the statistics available, they appear consistent with a Gaussian distribution. As previously stated, the  $\Delta\text{Log}_{10}(S2/S1)$  spectrum is dominated by recombination fluctuations, which are poorly understood, and thus more cannot be said in the absence of a larger calibration dataset. We calculate the predicted ER rejection in

TABLE II: The nuclear recoil acceptance  $A_{nr}$ , the efficiency  $\epsilon_{cut}$  of remaining nuclear recoil events after the *GammaX* cuts (see section VII), and the electron recoil rejection efficiency  $R_{er}$  for each of the seven energy bins. The predicted number of leakage events,  $N_{leak}$ , is based on  $R_{er}$  and the number of background events,  $N_{evt}$ , in each energy bin, for the 58.6 live-days WIMP-search data. Errors are the statistical uncertainty from the Gaussian fits on the electron recoil  $\Delta\text{Log}_{10}(S2/S1)$  distribution.

$E_{nr}$ (keV)	$A_{nr}$	$\epsilon_{cut}$	$1 - R_{er}$ ( $10^{-3}$ )	$N_{evt}$	$N_{leak}$
4.5 - 6.7	0.446	0.94	$0.8^{+0.7}_{-0.4}$	213	$0.2^{+0.2}_{-0.1}$
6.7 - 9.0	0.458	0.90	$1.7^{+1.6}_{-0.9}$	195	$0.3^{+0.3}_{-0.2}$
9.0 - 11.2	0.457	0.89	$1.1^{+0.9}_{-0.5}$	183	$0.2^{+0.2}_{-0.1}$
11.2 - 13.4	0.442	0.85	$4.1^{+3.6}_{-2.0}$	190	$0.8^{+0.7}_{-0.4}$
13.4 - 17.9	0.493	0.83	$4.2^{+1.8}_{-1.3}$	332	$1.4^{+0.6}_{-0.4}$
17.9 - 22.4	0.466	0.80	$4.3^{+1.7}_{-1.2}$	328	$1.4^{+0.5}_{-0.4}$
22.4 - 26.9	0.446	0.77	$7.2^{+2.4}_{-1.9}$	374	$2.7^{+0.9}_{-0.7}$
Total				1815	$7.0^{+1.4}_{-1.0}$

the case that  $\Delta\text{Log}_{10}(S2/S1)$  fluctuations are Gaussian. That is, we use the Gauss fits to the  $\Delta\text{Log}_{10}(S2/S1)$  spectrum in each of the seven energy bins to determine the energy-dependent discrimination power. The results are shown in Table II and Figure 34. Additionally, the expected number of background events in the WIMP acceptance window,  $N_{leak}$ , is shown, calculated on the basis of predicted rejection and background rate in the 58.6 live-days exposure (see Section VII).

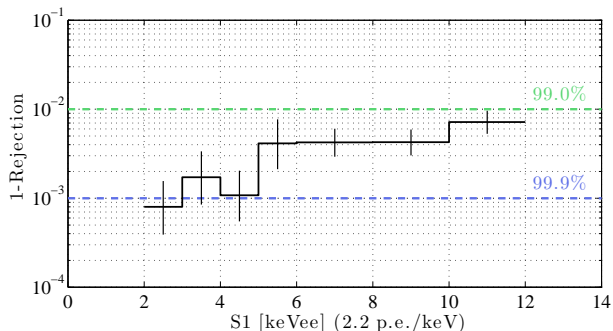


FIG. 34: The ER rejection as a function of S1 for  $\Delta\text{Log}_{10}(S2/S1) < \mu$ . The rejection improves at lower energies, to better than 99.9% in the range 2–3 keVee.

The observed trend of the ER rejection power with energy is unexpected. If recombination fluctuations were flat at all energies, or if the band widths were dominated by binomial fluctuations from light collection, photoelectron emission, etc., one would expect the band widths to grow at low energies, and hence the ER rejection power would deteriorate. The opposite is observed, and is due to two factors. First, the ER and NR bands themselves diverge slightly at lower energies, as first measured in [4]. Second, the width of the ER band does not grow at lower energies but instead remains relatively constant.

Figure 35 shows a decomposition of the ER band variance, using assumed statistical and instrumental fluctuations. It is quite evident that uncorrelated statistical and instrumental fluctuations cannot alone account for the observed degree of variance. Unfortunately, a model does not yet exist that successfully predicts recombination fluctuations in noble liquids, and hence more measurements are needed to reach a better understanding of the subject.

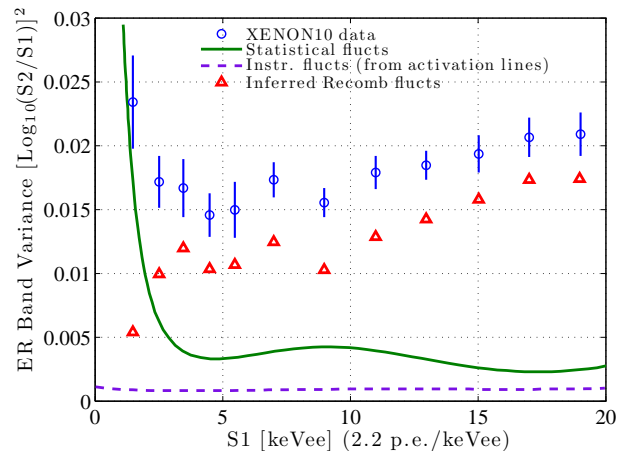


FIG. 35: (Color online) Decomposition of the ER band variance. The recombination fluctuations are inferred by comparing the expected statistical and instrumental fluctuations to the full observed band variance.

## VII. THE XENON10 DARK MATTER SEARCH DATA

The XENON10 Dark Matter Search data covered the period between October 6th 2006 and February 14th 2007. Figure 36 shows the accumulation of measurement livetime, interrupted by calibration runs. The global trigger rate was about 2.6 Hz with more than 92% livetime. A total of 74.7 live-days of data were collected. Of this, 16.3 were selected to be analyzed in order to define the event selections and cuts. The remaining 58.4 live-days were embargoed in order to carry out a blind analysis. The XENON10 results from this blind analysis have been published in [11, 12], and are referred to as blinded WIMP search data in the following.

### A. Background reduction with fiducial volume selection

Background events in XENON10 are dominated by electron recoils from radioactivity of detector materials. Due to the self-shielding of LXe, the background event rate falls dramatically from the edges to the center of the target. Based on Monte Carlo simulations and unblinded

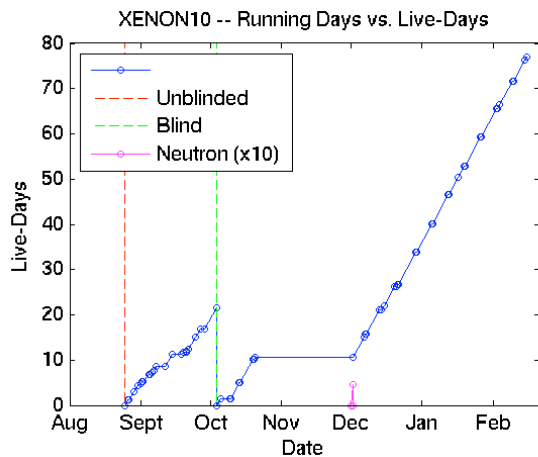


FIG. 36: (Color online) Running days vs live-days from XENON10 data-taking.

background data, a central fiducial volume was chosen to minimize background while maintaining the largest possible target mass. The fiducial volume was pre-defined for the blinded analysis with a radius of 80 mm and a drift time between 15 and 65  $\mu\text{s}$ , corresponding to a fiducial mass of 5.4 kg. Figure 37 shows the fiducial volume overlaid on the background rate distribution of single recoil events between 2-30 keVee (2.2 pe/keVee). Within the chosen fiducial volume, the overall background rate is reduced by almost a factor of 10, as shown in Figure 38.

A comparison between the measured background rate and the projected background from detailed Monte Carlo simulations, shown in Figure 39, reveals a dominant contribution from the stainless steel vessels, followed by approximately equal contributions from PMTs, feedthroughs, and Teflon. The contribution from intrinsic contamination of  $^{85}\text{Kr}$ , Rn,  $^{136}\text{Xe}$  in the liquid xenon, or nuclear recoils from ( $\alpha, n$ ) reaction or fission of  $^{238}\text{U}$  in the surrounding environment is subdominant or negligible in the entire WIMP search run. Details of the simulations and understanding of background contributions are discussed in Appendix A.

## B. Definition of anomalous events and cuts

During the analysis of both gamma calibration data and unblinded background data from XENON10, a class of anomalous single scatter events with smaller  $S2/S1$  ratio than that of normal single scatter electron recoil events were observed. These events produce a non-Gaussian tail extending into the acceptance region for nuclear recoils and to even lower  $S2/S1$  ratios. Most of these anomalous events are likely due to the coincidence of two gamma-ray interactions, where a single interaction occurs in the sensitive volume and at least one other interaction occurs in a region of the detector that

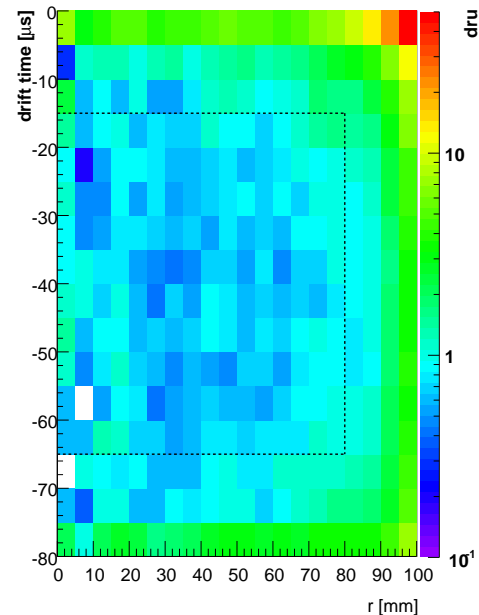


FIG. 37: (Color online) 2-30 keVee (based on S1 and 2.2 pe/keVee) event rate distribution in the fiducial volume as a function of the drift time and radius for the WIMP search run. The fiducial volume cut used in the final analysis is pre-defined based on the gamma calibration and unblinded WIMP search data and is indicated with the dashed lines.

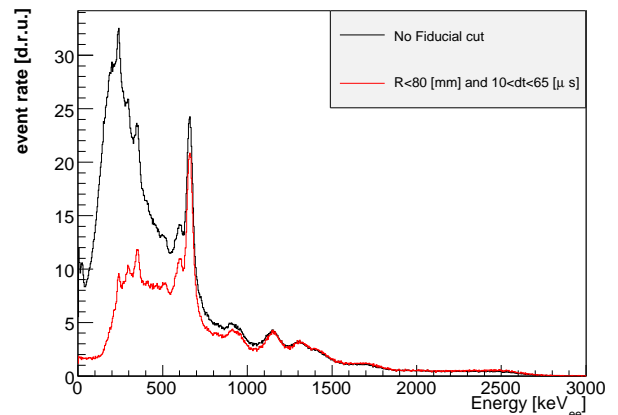


FIG. 38: (Color online) Overall XENON10 background energy spectrum before (black) and after (red) the fiducial volume cut. Here we use the combined energy scale.

is light-sensitive but not charge-sensitive. Such events, dubbed *Gamma-X*, may comprise two Compton scatters of a high-energy gamma-ray, or, e.g., coincident gamma-rays from a cascade, such as  $^{60}\text{Co}$  from the stainless steel cryostat. There are a few regions of the XENON10 detector that are light-sensitive but not charge-sensitive, such as the region between cathode and bottom PMTs or the

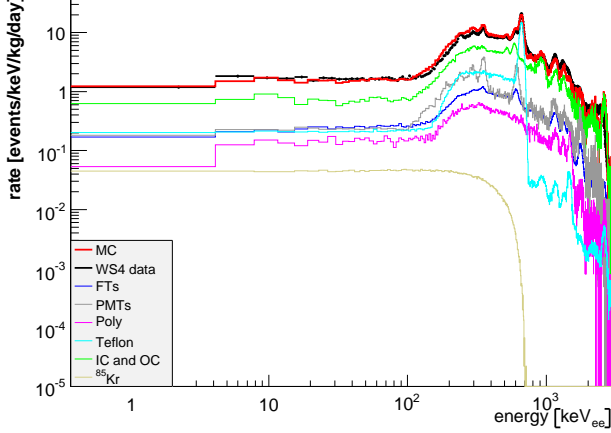


FIG. 39: (Color online) The measured XENON10 background event rate (black) compared to Monte Carlo simulations (red) in the 5.4-kg fiducial mass. The energy is based on combined energy scale. The contribution from different components from the main detector and shield are shown in different colors. FTs represent feedthroughs. Poly represents polyethylene in the shield. IC and OC represent internal cryostat and outer cryostat separately.

region around and below the bottom PMT array, as was shown in Fig. 23.

For illustration, Fig 40 shows the  $\Delta\text{Log}_{10}(S2/S1)$  vs. energy event distribution of the blinded WIMP search data. Prior to a final set of cuts, designed to remove these anomalous events, a total of 22 events is observed in the WIMP acceptance region. Only some of these events are expected from the statistical leakage of the electron recoil band. The spatial distribution of all events in the energy region of interest is shown in Fig 41.

Two cuts, based on the S1 hit pattern, were identified to remove these anomalous events. One cut is based on the asymmetry of S1 between the top and bottom array of PMTs, i.e.  $p_{asy} = (S1_t - S1_b)/(S1_t + S1_b)$ .  $p_{asy}$  is larger for anomalous events with some scatters in the region close to the top PMTs, but not in the sensitive LXe target. This cut also removes most of the events with misidentified S1 in software, e.g. a small S2 signal, or a micro-discharge pulse in the gas. Figure 42 shows the distribution of this parameter versus energy.

A second set of cuts is based on the S1 signal distribution on the top and bottom PMT arrays. We define a parameter  $p_{RMS} = \sqrt{\frac{1}{n} \sum (S1_i - \overline{S1})^2}$  from the Root-Mean-Square (RMS) value of the 5 (for top) or 10 (for bottom) PMTs receiving the largest hits. Anomalous events tend to give non-uniform S1-signal distributions, e.g., if one of the interactions occurs near the bottom PMT array. Figure 43 shows the effect of this cut for the bottom PMTs.

The above software cuts also remove a small fraction of genuine nuclear recoil events. By comparing the AmBe

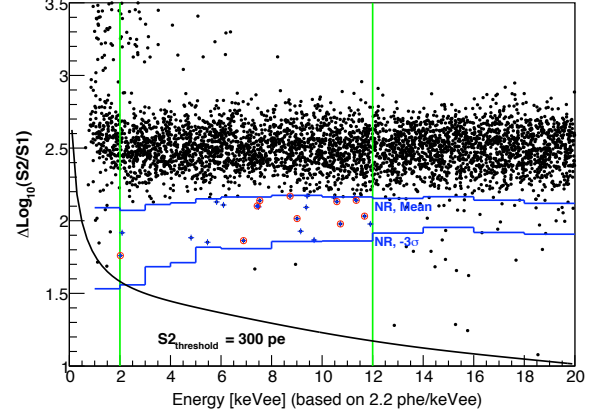


FIG. 40: (Color online) Event distribution in the  $\Delta\text{Log}_{10}(S2/S1)$  vs. Energy space for the 58.4-day WIMP search data. The crosses indicate the events that “leak” into the nuclear recoil acceptance region, which is within the mean and  $3\sigma$  of the nuclear recoil band. Red circles indicate the remaining events after all software cuts, discussed in the text.

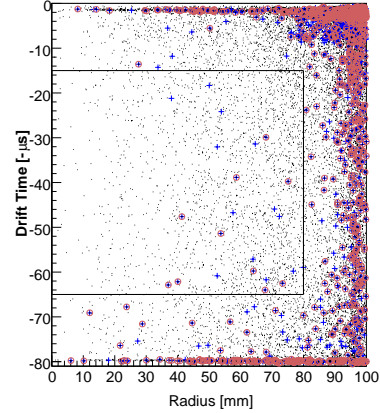


FIG. 41: (Color online) Event distribution in the 58.4-day WIMP search data. The crosses indicate the events that “leak” into the nuclear recoil acceptance region, as shown in Fig 40 in the energy window (2-12 keVee) of interest. Red circles indicate the remaining events after all software cuts, discussed in the text.

nuclear recoil data before and after the software cuts, the estimated cut efficiency  $\epsilon_{cut}$  was calculated and shown in Table II.

## Appendix A: The XENON10 Backgrounds

The particles potentially contributing to the background of the XENON10 detector are alphas, betas, gammas, and neutrons. Neutrons scattering with Xe nuclei yield nuclear recoils, possibly mimicking a WIMP sig-

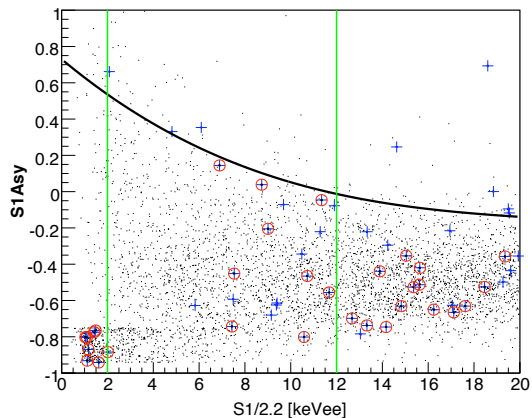


FIG. 42: (Color online) A cut based on the asymmetry of the S1 signal,  $p_{asy}$ , as discussed in the text. The crosses indicate the events that “leak” into the nuclear recoil acceptance region, as shown in Fig 40. The two vertical lines are the energy window of WIMP search. Red circles indicate the remaining events after all software cuts. The solid black curve is pre-defined to keep 98% electron recoil events. It removes 3 out of 22 “leakage events” in the energy window of interest (2-12 keVee).

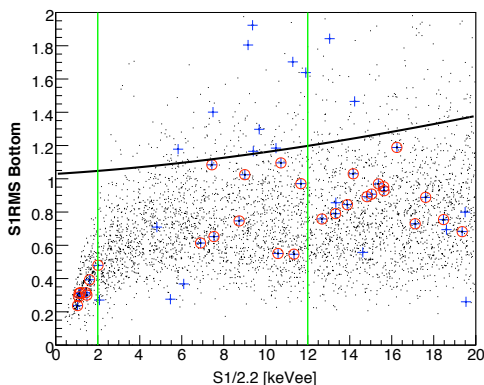


FIG. 43: (Color online) Cuts based on  $p_{RMSb}$  for the bottom PMTs, as defined in the text. The crosses indicate the events that “leak” into the nuclear recoil acceptance region, as shown in Fig 40. The two vertical lines are the energy window of WIMP search. Red circles indicate the remaining events after all software cuts. The solid black curve is pre-defined, which varies from 99% at 2 keVee and 90% at 20 keVee cut efficiency and fitted by the third-order polynomial function. It removes 9 out of 22 “leakage events” in the energy window of interest (2-12 keVee).

nal. Unless they are detected as multiple interactions in the sensitive volume, neutrons constitute an unrejectable background in the nuclear recoil band. Gamma and beta rays mostly populate the electron recoil band and constitute the most prominent background of the experiment. Alphas can contribute to background in the WIMP search region as they give rise to neutrons via  $\alpha$ -n

reactions in the detector materials.

### 1. Gamma and Neutron Backgrounds from Data and MC Simulations

Gamma and neutron backgrounds from the environment were studied to optimize the shield, and have been discussed in section III. After shielding, the dominant backgrounds in XENON10 result from radioactive contaminants in the detector and shield materials. These internal backgrounds were studied with material screening, using gamma-ray spectroscopy in a low count rate facility, with Monte Carlo simulations, and with the analysis of delayed coincidences in decay chains of radio-nuclides inside LXe. Simulations were based on the GEANT4 simulation toolkit [56], where the complete geometry of the detector and surrounding material was included.

As detailed in Table I, the shielding material and many detector construction components were screened with HPGe gamma spectrometers at the LNGS and SOLO screening facility [57]. The radioactive contamination of the screened material are listed in Table I (for the shield) and in the first row of table III (for the PMTs + bases). However, since XENON10 was a prototype experiment, the radioactivity of some detector components was not known. We used the minimum  $\chi^2$  method to extract the individual activities, by comparing the measured energy spectrum with the sum of the energy spectra for each radioactive decay chain within each material:

$$\chi^2 = \sum_{i=n}^N \frac{d_i - \sum_{j=1}^m F_{ij}(u_j U_j, th_j Th_j, k_j K_j, co_j Co_j, cs_j Cs_j)}{d_i} \quad (\text{A1})$$

where  $n$  and  $N$  are the first and last bin of the energy spectra, defining the fit range. Here we use a bin width of 3.75 keV,  $n = 50$ , and  $N = 450$ .  $d_i$  is the rate in the  $i^{th}$  bin of the measured energy spectrum, and  $F_{ij}$  is the corresponding expected rate from simulated backgrounds in material  $j$ ;  $m = 41$  is the total number of simulated materials;  $u_j$ ,  $th_j$ ,  $k_j$ ,  $co_j$  and  $cs_j$  are the scaling parameters related to nominal activities of material  $j$  in  $^{238}\text{U}$  ( $U_j$ ),  $^{232}\text{Th}$  ( $Th_j$ ),  $^{40}\text{K}$  ( $K_j$ ),  $^{60}\text{Co}$  ( $Co_j$ ), and  $^{137}\text{Cs}$  ( $Cs_j$ ), respectively. The minimization is done by the MINUIT routines in ROOT [45].

The results of this fit procedure are summarized in table III. The main component to the background energy spectrum of XENON10 originates from a  $^{137}\text{Cs}$  peak at 662 keV. Fig. 44 shows the 662 keV peak decreasing at smaller radii, a clear indication that it is not diluted in the LXe. A study of the spacial distribution of events in this peak shows that the  $^{137}\text{Cs}$  source is all around the detector edges. Thus a surface contamination of the anthropogenic  $^{137}\text{Cs}$  has to be assumed, either on the inner cryostat can or on the Teflon. The best fit results localize the  $^{137}\text{Cs}$  on the Teflon, with a total activity of  $5.73 \pm 0.57$  Bq.

TABLE III: Radioactive contaminations of material used in the construction of the XENON10 detector, as obtained from screening (PMTs, bases and polyethylene shield) and by comparing the low-background data to MC simulations.

Sample	Mass or number (M)	$^{238}\text{U}$ mBq/M	$^{232}\text{Th}$ mBq/M	$^{40}\text{K}$ mBq/M	$^{60}\text{Co}$ mBq/M	$^{137}\text{Cs}$ mBq/M	$^{85}\text{Kr}$ mBq/M
PMTs + bases	89 pieces	0.32	0.23	8.6	1.7	1.0	
Inner cryostat	37.4 kg	130	470	310	65	8.1	
Outer cryostat	144.7 kg	80	120	39	24	8.0	
Polyethylene	1540 kg	1.2	0.3	11.6	0.01	1.0	
Teflon (TPC)	6.26 kg	1.1	4.8	48	0.01	910	
3 Feedthroughs	1.758 kg	130	28	270	30	13	
Xenon	14.5 kg						1.0

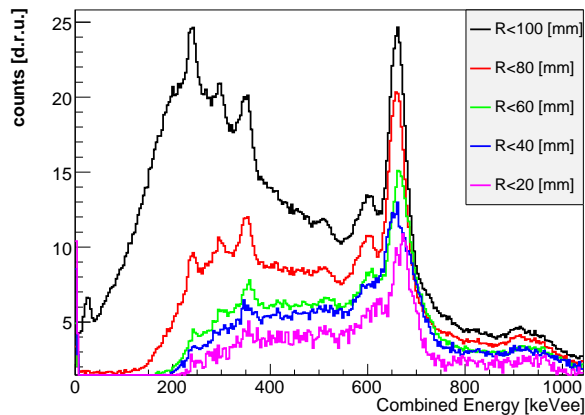


FIG. 44: (Color online) Energy spectrum of background events in XENON10 with different radial cuts, with a focus on the  $^{137}\text{Cs}$  peak.

The main source of neutrons in XENON10 are  $(\alpha, n)$  and spontaneous fission reactions from  $^{238}\text{U}$  and  $^{232}\text{Th}$  in the detector and shield material. Another source of neutrons are spallation and photo-nuclear reactions of cosmic ray muons in the rock and shield. As explained in Section III, the neutrons from outside the shield are stopped or thermalized by the polyethylene.

Using the  $^{238}\text{U}$  and  $^{232}\text{Th}$  activities as given in Table III, the energy spectra and number of expected neutrons from  $(\alpha, n)$  and spontaneous fission reactions in each material has been calculated with the modified SOURCES4A code [58]. These are given in Table IV (second column).

The neutrons are then propagated into the sensitive region using the GEANT4 code and detector geometry. In figure 45 the predicted single scattering nuclear recoil energy spectrum from the neutrons from all the material considered in the simulation is shown, together with the individual contributions from all the material. The number of predicted single nuclear recoils in the WIMP search region is shown in Table IV (third column), along with the total number of single nuclear recoils (fourth column).

The total rate of single nuclear recoils in the energy region from 2 to 12 keV<sub>ee</sub> is expected to be  $1.67 \times 10^{-3}$  event/kg/day, i.e. for an exposure of 5.4 kg  $\times$  58.6 days, the total number of nuclear recoils expected from the contamination of the XENON10 detector material is less than 0.53 events [11].

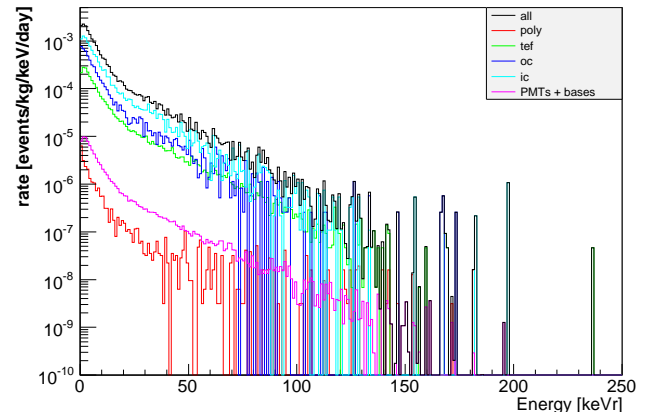


FIG. 45: (Color online) Monte Carlo simulation of total nuclear recoil spectrum expected from the neutrons produced in all the material considered (black), along with the individual contributions from each material.

## 2. Intrinsic backgrounds in LXe

Delayed coincidence analyses to determine the Radon, Thoron, U/Th and  $^{85}\text{Kr}$  concentration in the LXe have been carried out by looking at the specific decay signatures. For Radon, the consecutive beta-alpha decays occurring in the decay of  $^{214}\text{Bi}$  (shown in Eq. A2) are required to occur within the same waveform, in the same time order as in the decay scheme and with the proper energies ( $E_\beta < 3000$  keV and  $E_\alpha > 6500$  keV). With these cuts, the residual accidental coincidences are negligible and the events surviving the cuts are taken as real  $^{214}\text{Bi}$  decays. The resulting Rn concentration in LXe, considering the detection efficiency and the efficiency of above cuts, is  $(59 \pm 2) \mu\text{Bq/kg}$ . For  $^{220}\text{Rn}$  arising from the  $^{232}\text{Th}$

TABLE IV: Neutron fluxes (second column) calculated with the modified SOURCES4A code, using the activities in  $^{238}\text{U}$  and  $^{232}\text{Th}$  given in table III. Column 3 lists the number of single nuclear recoils expected in the WIMP search region of interest, inside the fiducial volume, for each material. Column 4 lists the total number of single nuclear recoils expected in the whole volume.

Material	Flux [neutron/sec]	nuclear recoil evt/kg/day	total nuclear recoil evt/kg/day
Teflon	$9.60 \times 10^{-6}$	$5.34 \times 10^{-4}$	$3.69 \times 10^{-4}$
Poly	$5.22 \times 10^{-6}$	$2.38 \times 10^{-6}$	$7.32 \times 10^{-7}$
OC	$5.64 \times 10^{-5}$	$2.82 \times 10^{-4}$	$1.88 \times 10^{-4}$
IC	$4.38 \times 10^{-5}$	$5.57 \times 10^{-4}$	$4.02 \times 10^{-4}$
PMT	$2.41 \times 10^{-8}$	$1.13 \times 10^{-4}$	$5.16 \times 10^{-4}$
Base	$3.81 \times 10^{-6}$	$1.80 \times 10^{-4}$	$6.39 \times 10^{-5}$

chain, the time window for the events is much shorter, namely  $3 \mu\text{s}$  versus the maximum time acquisition window, i.e.  $80 \mu\text{s}$ , and the energy of the two particles has to be  $E_\beta < 2400 \text{ keV}$  and  $E_\gamma > 7000 \text{ keV}$ . The resulting concentration of  $^{220}\text{Rn}$  in LXe is  $(4.7 \pm 0.2) \mu\text{Bq/kg}$ . For both Radon and Thoron the events are distributed mainly in the outermost LXe region, suggesting that both radioisotopes emanate mainly from the surface of the teflon vessel or inner stainless steel chamber.

The delayed coincidence technique has also been used to estimate the Krypton concentration in LXe, by tagging the beta-gamma decay mode (0.434 % branching ratio) of the  $^{85}\text{Kr}$  diluted in the liquid.  $^{85}\text{Kr}$ , which has a concentration about  $10^{-11}$  in Kr, is a beta emitter that produces background in the LXe volume. XENON10 experiment requires the Kr/Xe contamination to be less than 10 ppb, which gives about 0.2 dru electron recoil background. To have this low Kr/Xe contamination level, the Xe gas used for XENON10 was purified by the Spectra Gases company [59] in several passages through a large cryogenic distillation column. Figure 46 shows the energy spectra of the gamma and beta particles selected by the cuts. A total of 59 delayed-coincidence events were found in the entire WIMP-search data. Taking into account the detection efficiency of these events, we determine an  $^{85}\text{Kr}$  activity of  $(1.0 \pm 0.06) \text{ mBq/kg}$ , which translates into  $(5.0 \pm 0.3) \text{ ppb}$  of natural Kr/Xe contamination for typical atmospheric  $^{85}\text{Kr}$  abundances. This value is compatible with the value quoted by the Xe gas supplier [59] and is sufficiently low for XENON10.

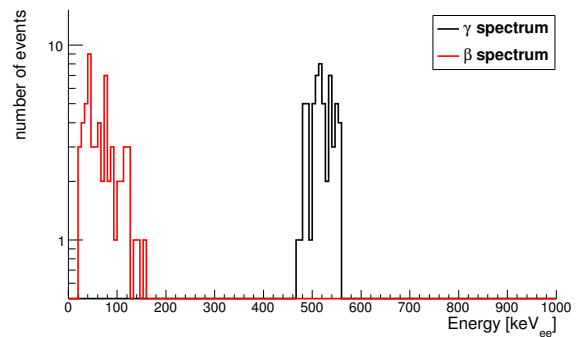
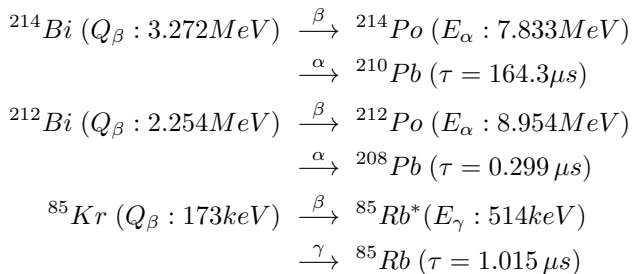


FIG. 46: (Color online) Gamma and beta energy spectra of the  $^{85}\text{Kr}$   $\beta - \gamma$  decay (0.434% BR) from the XENON10 data, after delayed coincidence cuts.

## Acknowledgments

This work was supported by the National Science Foundation under grants No. PHY-03-02646 and PHY-04-00596, and by the Department of Energy under Contract No. DE-FG02-91ER40688, the CAREER Grant No. PHY-0542066, the Volkswagen Foundation (Germany) and the FCT Grant No. POCI/FIS/60534/2004 (Portugal). We thank the Director of the Gran Sasso National Laboratory, Prof. E. Coccia, and his staff for support throughout this effort. Special thanks go to the Laboratory engineering team, led by P. Aprili, and to F. Redaelli of COMASUD for their contribution to the XENON10 installation. We are also thankful to M. Laubenstein for the radioactivity screening of the many XENON10 materials.

[1] E. Aprile *et al.* (XENON Collaboration), *New Astr. Rev.* **49**, 289 (2005).

[2] E. Aprile, K. L. Giboni, P. Majewski, K. Ni, M. Ya-



- mashita, 2004, IEEE Trans, No.5, 1986.
- [3] E. Aprile, K.L. Giboni, P. Majewski, K. Ni, M. Yamashita, R. Hasty, A. Manzur, D. McKinsey, Phys. Rev. D. **72**, 072006 (2005).
- [4] E. Aprile *et al.*, Phys. Rev. Lett. **97**, 081302 (2006).
- [5] K. Ni, "Development of a Liquid Xenon Time Projection Chamber for the XENON Dark Matter Search", Ph.D. Thesis (2006), Columbia University, New York.
- [6] E. Aprile, A. Curioni, K. L. Giboni, M. Kobayashi, U. G. Oberlack and S. Zhang, Nucl. Instrum. Meth. A **593**, 414 (2008) [arXiv:0805.0290 [physics.ins-det]].
- [7] J. Adam *et al.* [MEG collaboration], arXiv:0908.2594 [hep-ex].
- [8] K. Giboni, E. Aprile, T. Doke, S. Suzuki, L. M. P. Fernandes, J. A. M. Lopes and J. M. F. dos Santos, JINST **2**, P10001 (2007).
- [9] T. Haruyama *et al.*, in: *Cryocoolers 13*, Springer, New York, 689 (2005).
- [10] Gran Sasso National Laboratory, INFN, Italy. <http://www.lngs.infn.it/>.
- [11] J. Angle *et al.* (XENON Collaboration), Phys. Rev. Lett. **100**, 021303 (2008).
- [12] J. Angle *et al.* (XENON Collaboration), Phys. Rev. Lett. **101**, 091301 (2008).
- [13] J. Jortner, *et al.*, J. Chem. Phys. **42**, 4250 (1965).
- [14] S. Kubota, *et al.*, Phys. Rev. B **17**, 2762 (1978).
- [15] E. Aprile [XENON100 Collaboration], AIP Conf. Proc. **1166**, 205 (2009).
- [16] XMASS project, <http://www-sk.icrr.u-tokyo.ac.jp/xmass/>.
- [17] LUX project, <http://lux.brown.edu/>.
- [18] A.I. Bolozdynya, Nucl. Instrum. Meth. A **422** 314 (1999).
- [19] C.M.B. Monteiro, *et al.*, JINST **2**, P05001 (2007).
- [20] E. Aprile and T. Doke, arXiv:physics.ins-det/0910.4956.
- [21] V.N. Solovov, *et al.*, Nucl. Instr. and Meth. A **516**, 462 (2004).
- [22] E. Aprile *et al.*, "The XENON Dark Matter Project", proposal submitted to National Science Foundation (2001).
- [23] P. Shagin *et al.*, Nucl. Instr. and Meth. A **556**, 215 (2006).
- [24] K. Ni *et al.*, Nucl. Instr. and Meth. A, **551**, 356 (2005).
- [25] F. Sauli, Nucl. Instr. and Meth. A, **386**, 531 (1997).
- [26] E. Aprile *et al.*, Proceedings of the 2005 IEEE International Conference on Dielectric Liquids (ICDL 2005), p. 345-348, July 2005.
- [27] E. Aprile *et al.*, Nucl. Instrum. Meth. A **338**, 328 (1994).
- [28] M. Yamashita *et al.*, Nucl. Instrum. Meth. A **535**, 692 (2004).
- [29] <http://www.caen.it/nuclear/>
- [30] <http://www.heinzinger.com/>
- [31] <http://www.hamamatsu.com/>
- [32] H. Neder, G. Heusser and M. Laubenstein, Appl. Radiat. Isot. **53**, 225 (2000).
- [33] C. Arpesella, Appl. Radiat. Isot. **47**, 991 (1996).
- [34] <http://www.kyocera.com/>
- [35] <http://www.saesgetters.com/>
- [36] <http://www.knf.com/>
- [37] <http://www.fonderie-de-gentilly.com/>
- [38] P. Belli, *et al.*, Nuovo Cimento A **101**, 959 (1989).
- [39] H. Wulandari *et al.*, Astropart. Phys. **22**, 313-322 (2004).
- [40] P. Sorensen, "A Position-Sensitive Liquid Xenon Time-Projection Chamber for Direct Detection of Dark Matter," Ph.D. Thesis (2008), Brown University, Providence RI.
- [41] L. de Viveiros, "Optimization of Signal versus Background in Liquid Xe Detectors used for Dark Matter Direct Detection Experiments", Ph.D. Thesis (2009), Brown University, Providence RI.
- [42] <http://www.durridge.com/RAD7.htm>
- [43] T. Doke *et al.*, Nucl. Instrum. Meth. A **420** 62 (1999).
- [44] <http://www.struck.de/sis3301.htm>
- [45] <http://root.cern.ch>
- [46] C.E. Dahl, "The physics of background discrimination in liquid xenon, and first results from Xenon10 in the hunt for WIMP dark matter," Ph.D. Thesis (2009), Princeton University, Princeton NJ.
- [47] T. Doke, Nucl. Instr. and Meth. **196**, 87 (1982).
- [48] G. Bakale, U. Sowada and W.F. Schmidt, J. Phys. Chem. **80** (1976) 2556.
- [49] L.M. Bakov, *et al.*, Nucl. Instr. Meth. A **379** (1996) 482.
- [50] scattering length reference.
- [51] K. Ni *et al.*, Nucl. Instr. Meth. A **582** (2007) 569.
- [52] E. Conti *et al.* [EXO Collaboration], Phys. Rev. B **68**, 054201 (2003). arXiv:hep-ex/0303008.
- [53] E. Aprile *et al.*, Phys. Rev. B **76**, 014115 (2007). arXiv:0704.1118 [astro-ph].
- [54] T. Shutt *et al.*, Nucl. Instr. Meth. A **579** (2007) 451.
- [55] ESTAR: stopping power and range tables for electrons. <http://physics.nist.gov/PhysRefData/Star/Text/ESTAR.html>.
- [56] S. Agostinelli *et al.*, Nucl. Instrum. Meth. A **506**, 250 (2003). <http://geant4.cern.ch/>
- [57] M. Attisha *et al.* Topical Workshop on Low Radioactivity Techniques (LRT 2004), AIP **785**, 75-78 (2005).
- [58] M. Carson *et al.*, Astrop. Physics **21** (2004) 667.
- [59] <http://www.spectragases.com/>